DTU Library

Exploring the Influence of Composition and Morphology on the oxygen evolution reaction Performance of Co-Based Catalysts

Poureshghi, Fatemeh; Seland, Frode; Jensen, Jens Oluf; Heath, Megan Muriel; Sunde, Svein

Link back to DTU Orbit

Exploring the influence of composition and morphology on the oxygen evolution reaction performance of Co-based catalysts

Fatemeh Poureshghi [a],[*], Frode Seland [a], Jens Oluf Jensen [b], Megan Muriel Heath [c], Svein Sunde [d]

[a] Department of Materials Science and Engineering, Norwegian University of Science and Technology (NTNU), N-7491 Trondheim, Norway
[b] Department of Energy Conversion and Storage, Technical University of Denmark, DK-2800 Kgs. Lyngby, Denmark
[c] Department of Materials Science and Engineering, Norwegian University of Science and Technology (NTNU), N-7491 Trondheim, Norway
[d] Department of Materials Science and Engineering, Norwegian University of Science and Technology (NTNU), N-7491 Trondheim, Norway

ARTICLE INFO

ABSTRACT

Efficient catalysts for the oxygen evolution reaction (OER) are essential for advancing renewable energy technologies. This study focuses on the synthesis and characterization of Co_xP_y, CoO, CoP, NiCoP, and NiCo/C nanoparticles as catalysts for the oxygen evolution reaction (OER). The Co_xP_y nanoparticles exhibited a sea-urchin-like morphology, providing a high surface area for electrocatalytic activity. Other catalysts exhibited distinct morphologies, including spherical particles and porous structures. Characterization techniques, such as transmission electron microscopy and X-ray diffraction, confirmed the morphology and composition of the synthesized nanoparticles. The electrocatalytic performance of the catalysts was evaluated through polarization curve measurements, and a microkinetic steady-state model based on the Electrochemical Oxide Path was developed to understand the OER mechanism. The impact of adventitious Fe on catalyst activity was also investigated, revealing the high sensitivity of Co_xP_y to Fe. The findings suggest the dominance of the Electrochemical Oxide Path in the OER mechanism for all catalysts, with NiCoP showing the lowest onset potential.

1. Introduction

Electrolytic water splitting into hydrogen and oxygen is considered a clean and feasible approach for developing a carbon-free economy [1–3]. Water oxidation ($2 H_2O \rightarrow O_2 + 4 H^+ + 4e^-$), also known as the oxygen evolution reaction, OER), is recognized as a major bottle-neck in water splitting, due to its sluggish kinetics [4,5]. In the early stages of catalyst development, noble metal oxides such as RuO_2 and IrO_2 were developed as the most effective catalysts [6,7] for proton exchange membrane (PEM) electrolyzers. Nonetheless, the extent to which these can be used is seriously limited by small reserves and high cost, which puts a cap on industry-scale applications [7,8]. It is thus of great importance to develop cheap, earth-abundant, and efficient OER electrocatalysts. Nanocatalysts based on non-precious metals have been subjected to intense study because of their low cost and abundance [9–11]. Among them, 3*d* transition metal oxides, including those based on Co, have been employed extensively as OER catalysts in alkaline media [12]. However, their further development into efficient OER electrocatalysts is frequently hindered by insufficient electronic conductivity [13] and low surface area [14], especially for Co-based oxides.

To increase the number and efficiency of catalytic sites as well as to enhance the conductivity, the construction of elaborate nano-architectures have been pursued [15–17]. Meanwhile, the addition of a second metal such as Ni and Fe has been considered as a promising strategy to improve the electrocatalytic activity [18–21].

Despite the significant interest in an observed enhancement of OER activity with Fe incorporation in for example Ni catalysts, the role of Fe during OER catalysis remains under intense debate [22–24]. For example, DFT calculations carried out by Friebel *et al.* [23] indicate that Fe^{3+} cations in $Ni_{1-x}Fe_xOOH$ would have a lower OER overpotential than Ni^{3+} cations. On the other hand, Li *et al.* [24] have suggested that Fe^{3+} acts as a Lewis acid and promotes the formation of Ni^{4+}, which then leads to the enhanced OER activity.

Mixed Ni − Co oxides and (oxy)hydroxides were studied as electrocatalysts for the OER by Tseung *et al.* [25] already in 1977. However, since in many cases, the presence of Fe impurities have not been addressed and a number of different preparation methods have been applied for making the catalysts, a fundamental understanding of the effects on the OER of mixing these two elements remains inconclusive. For example, an enhancement of the OER activity for $NiCo_2O_4$ compared

---

* Corresponding author.
  E-mail address: fatemeh.poureshghi@nord.no (F. Poureshghi).

to Co_3O_4 or NiO electrocatalysts was reported by Jasem and Tseung [26], but without mentioning the possible effects of Fe impurities on these electrocatalysts. On the contrary, Guo and coworkers found that Co-rich compositions that contained Ni were more active than $Co(OH)_2$ and Ni-rich compositions [27].

Since different preparation methods may lead to very different results in terms of catalyst architecture, impurities, etc., the existence of a wide variety of such methods is in itself also an obstacle to a fundamental understanding of the mixed Ni − Co oxides and (oxy)hydroxides. For example, depending on whether the catalyst material is an oxide [10,28–30] or an (oxy)hydroxides [31–33], significantly different electrochemical active surface areas will be obtained, which may be difficult to compensate for when comparing different catalyst. Other studies have shown that the morphology of the catalyst can also affect the catalytic activity [27,31,34]. Other factors may also compound the direct comparison of different catalysts, for example when these are performed at rotating-disc electrodes. The use of binders (e.g. Teflon or Nafion™) to prepare powder-catalyst electrodes has been shown to influence catalytic activity of mixed Ni-Co oxides/hydroxides [26,35]. Additionally, the use of supports such as N-doped graphene [36], reduced graphene oxide [37], and metal-organic frameworks [38] may complicate a fundamental understanding of the roles of Co and Ni in catalysis.

Among the various Ni- and Co-based materials that have been developed as efficient electrocatalysts for water oxidation, metal phosphides (M_xP_y) have received attention because of their excellent catalytic activity. However, phosphorus-rich transition metal phosphides (x < y) contain significant phosphorus-phosphorus bonding and are usually unstable [39]. There are several reports in which various catalyst supports such as reduced graphene oxide (rGO) have been used to increase the stability of phosphorus-rich M_xP_y electrocatalysts [40–42]. For example, Wang *et al.* [40] reported a novel electrocatalyst based on CoP_2 nanoparticles for overall (i.e. HER and OER) water splitting. To enhance the stability of CoP_2 nanoparticles, these were supported on reduced graphene oxide (rGO) to form CoP_2/rGO nanocomposites. Despite this drawback regarding poor stability of phosphorus-rich transition metal phosphides, the promising activity and relatively higher stability of metal-rich M_xP_y compositions make them worth pursuing in an attempt to combine high activity and stability, which would make them prime candidates as electrocatalysts for overall water electrolysis (both hydrogen and oxygen evolution reactions).

In recent years, the field of electrocatalysis has witnessed significant advances, not only in experimental approaches but also in computational methodologies based on artificial intelligence (AI). However, these methods, such as those based on Bayesian optimization [43], still require patterns and information from which they can infer better catalysts. Therefore, delineating systematically the performance of catalysts, such as those investigated here, is needed also for providing the input on which machine learning will depend.

In this work, we focus on the synthesis and characterization of CoO, Co_xP_y, NiCoP, and NiCo/C nanoparticles as efficient electrocatalysts for the OER.

The key differentiating factor of our work lies in the unique sea-urchin-like morphology observed for the Co_xP_y nanoparticles. This distinct morphology provides a very large area, allowing for enhanced electrocatalytic performance. Previous studies have primarily focused on monometallic catalysts or different morphology, such as nanoparticles or thin films. However, the sea-urchin-like structure of Co_xP_y nanoparticles has not been extensively explored for the OER.

Moreover, our study employs a comprehensive characterization approach, including scanning electron microscopy (SEM), transmission electron microscopy (TEM), X-ray diffraction (XRD), and electrochemical impedance spectroscopy (EIS), to elucidate the morphology, crystal phases, and electrochemical properties of the catalysts. This thorough characterization allows for a detailed understanding of the structure-activity relationship and provides valuable insights into the catalytic performance.

Furthermore, a microkinetic modeling approach is employed to support the proposed mechanism, namely the Electrochemical Oxide Path, for the OER on these catalysts. This modeling provides a theoretical framework to explain the observed experimental results and elucidate the underlying reaction kinetics.

By investigating the effect of adventitious Fe on the catalyst activity, we reveal that Co_xP_y nanoparticles are highly sensitive to Fe. Moreover, it highlights the importance of understanding the interaction between catalysts and impurities in electrolyte solutions.

2. Experimental

2.1. Materials

Oleylamine (OAm; technical grade, 70%), tri-n-octylphosphine (TOP; 97%), nickel(II) acetylacetonate ($Fe(acac)_3$; 97%), iron(II) acetylacetonate ($Ni(acac)_2$; anhydrous, 95%) Toluene (anhydrous, 99.8%), acetone (99.5%) and isopropanol (IPA; 99.5%), potassium hydroxide (99.99%), nafion (5%). All chemicals were purchased from Sigma-Aldrich and used as received, without further purification. Deionized water (DI-water), generated in a Milli-Q water system 18.2 MΩ cm, was used for all measurements.

2.1.1. Synthesis of cobalt oxide nanoparticles

All synthesis was carried out in a dry, oxygen-free, Ar atmosphere by employing standard Schlenk line and glove box techniques. The equivalent was defined as the ratio of mmol of each precursor to the total mmol of metal precursor (15.6).

For the synthesis of CoO nanoparticles, 50 mL of OAm (156 mmol, 10 equiv) was added to a 250 mL three-neck round bottom flask and evacuated for 10 min at room temperature. In the next step, $Co(acac)_2$ (15.6 mmol, 1 equiv), and TOP (14 mL, 2 equiv) were added to the solution and kept at 50°C for 5 min under Ar atmosphere (99.9999%) then temperature was ramped to 230°C at rate of 8°C min^{-1} and kept at this temperature for 2 h. After heating, the flask was left to cool to room temperature either gradually while it was kept inside the heating mantle or with the heating mantle removed immediately after synthesis. The black product was dissolved in the mixture of IPA and toluene and precipitated by centrifuging subsequently. This dispersion and precipitation was carried out at least three times to obtain surface-cleaned nanoparticles. The final precipitate was dried under vacuum drying at 60°C overnight.

2.1.2. Synthesis of nickel cobalt nanoparticles supported on carbon

The same synthesis procedure described for CoO nanoparticles was applied for the synthesis NiCo Nanoparticles Supported on Carbon (NiCo/C), in which 7.8 mmol $Ni(acac)_2$, 7.8 mmol $Co(acac)_2$ and 2 g Vulcan XC-72 carbon black were added to the flask at the outset of the reaction.

2.1.3. Synthesis of binary cobalt phosphide and ternary nickel cobalt phosphide nanoparticles

The protocol developed to synthesize Co_xP_y and NiCoP nanoparticles is based on the method refined by Muthuswamy *et al.* [44] for the synthesis of discrete Ni_2P phase-pure nanoparticles. Formation of Co_xP_y and NiCoP nanoparticles were achieved by further heating the metallic solution precursor which was prepared via the procedure described above at 350°C for 30 min. The final product was washed and dried with a similar procedure described for metallic nanoparticles.

2.2. X-ray powder diffraction and rietveld refinement

Powder X-ray diffraction (PXRD) was carried out on a Bruker D8 A25 DaVinci X-ray Diffractometer with Cu Kα radiation (Billerica, Massachusetts, USA). Samples were deposited onto zero background silicon sample holders and analyzed in the 2θ range between 20° and 80° with a

step size of 0.04° and a collection time of 6 s. Identification of phases was made by comparison to the powder diffraction files (PDFs) of the International Center of Diffraction Data (ICDD) using Eva 5.1 software. For easier phase identification, the background was subtracted using EVA software.

2.3. Scanning transmission electron microscopy

Scanning transmission electron microscopy (S(T)EM) was carried out on a Hitachi S-5500 FESEM (Krefeld, Germany) equipped with an INCA 350 energy dispersion X-ray (EDS) analysis unit. Acceleration voltages of 30 kV and 20 kV were used for the images and the analyses, respectively. All samples were prepared by dropping a toluene suspension containing uniformly dispersed nanoparticles on a carbon film supported on a 300-mesh copper grid.

2.4. Transmission electron microscopy (TEM)

TEM bright-field, TEM high-angle annular dark-field imaging (HAADF), and TEM-EDS were performed using a spherical aberration-corrected JEOL 2100 F operating at 200 kV. EDS mapping was performed using JEOL Silicon Drift Detector (DrySD60GV: sensor size, 60 m) with a solid angle of approximately 0.5 sr.

2.5. X-ray photoelectron spectroscopy

Spectra were collected on a Omicron Argus X-ray photoelectron spectrometer, using a Mg Kα (hν = 1486.6 eV) radiation source having a 300 W electron beam power. The samples were analyzed under ultra-high-vacuum conditions 8–10 Pa. After recording a broad range spectrum (pass energy, 100 eV), high-resolution spectra were recorded for the C 1s, Ni 2p, Co 2p and P 2p core XPS levels (pass energy, 200 eV). The binding energies were calibrated with respect to the C 1s peak at 284.8 eV. Spectrum processing was carried out using the Casa XPS software package.

2.6. Raman spectroscopy

Raman spectroscopy was carried out using a WITec alpha 300 R Confocal Raman device equipped with a 532 nm laser. Raman spectra were obtained after 20 accumulations for 20 s from 100 to 1250 cm^{-1}.

2.7. Electrochemical characterization

Electrochemical characterization was carried out in a standard three-electrode rotating disc electrode (RDE) setup from Pine Instruments. Polished glassy carbon (GC) electrodes were used as working electrodes (A = 0.196 cm^2, Pine Instruments) and a Pt foil was used as a counter electrode, measured versus a Hg|HgO filled with 4.2 mol dm^{-3} from Pine Instruments as a reference electrode. Polytetrafluoroethylene (PTFE) containers were used both for electrochemical experiments and electrolyte preparation. All measurements were controlled using a Bio-Logic Potentiostat/Galvanostat (Model VMP3) in 0.1 and 1 mol dm^{-3} KOH (99.99% and 85% trace metal basis). Cyclic and linear sweep voltammograms were collected at a rotation speed of 1600 rpm. Tafel data were collected in the electrolyte using chronoamperometry technique with E$_{appl}$ stepped from 1.4 to 1.7 V in 20 mV increments. At each potential step, steady-state data were collected at rotation rates (ω) of 2000 and 600 rpm; data were also collected in the absence of disk rotation. Catalyst inks were prepared by dispersing 2.5 mg of the catalyst powders in a mixture of 750 \µL of m-Q, 250 \µL of 2-propanol, and addition of 50 \µL of Nafion (5 wt%). The inks were homogeneously dispersed by ultrasonication for 20 min and then 10 \µL was drop-casted on the GC electrode to make up a final metal loading of 0.12 mg cm^{-2}. All electrochemical data were corrected for uncompensated series resistance after data collection. The uncompensated resistance of the cell was

measured with a single-point high-frequency impedance measurement, and IR drop was compensated at 85% through positive feedback using the Bio-Logic EC-Lab software. Our typical electrochemical cell had R$_u$ ~ 4–5 Ω in 1 mol dm^{-3} KOH. Electrochemical impedance spectroscopy measurements were carried out in five different overpotentials (0.6 V vs. Hg/HgO from 100 Hz to 1 MHz with an amplitude of 10 mV. R$_u$ is taken as the minimum impedance at a phase angle closest to zero at high frequency.

Double layer capacitance was estimated to determine the electrochemically active surface area (ECSA) as previously described [5]. In brief, a potential range in which there is minimal faradaic current response was estimated by CV. All the measured current in this region is assumed to be a charging current due to double-layer charging. CV measurements were conducted in a quiescent solution by sweeping the potential across this non-faradaic region 1.1–1.2 V from the more positive to negative potential and back at 8 different scan rates: 10, 30, 50, 70, 100, 200, and 300 mVs^{-1}. The working electrode was held at each potential vertex for 10 s before beginning the next sweep [45,46]. Plotting the charging current as a function of the scan rate yields a straight line with a slope equal to the double-layer capacitance.

2.8. Calibration of Hg/HgO reference electrode and conversion to RHE

The calibration of Hg/HgO electrode was performed in a standard three-electrode system with polished Pt foil as the working and counter electrodes, and a Hg/HgO electrode as the reference electrode. Electrolytes were pre-purged and saturated with 99.9999%H$_2$/Ar. Linear sweep voltammetry (LSV) was then performed at a scan rate of 0.5 mV s^{-1}, and the potential at which the current crossed zero is considered to be the thermodynamic potential for the hydrogen electrode reactions. For example, in 1 mol dm^{-3} KOH, the zero current point appeared at 0.900 V, and so the potential with respect to the reversible hydrogen electrode (RHE) is given by *E*(RHE) = *E*(Hg/HgO) + 0.900 *V*.

3. Results and discussion

3.1. Characterization of CoO nanoparticles

Fig. 1 b, 1g, and 1a show the TEM images, EDS mapping, and XRD pattern of the synthesized CoO nanoparticles. As shown in the XRD pattern (Fig. 1a), the characteristic peaks located at 2θ = 36.54, 42.44, 61.53, 73.82 and 77.66° match the (111), (200), (220), (311) and (222) plane of bulk face-centered cubic (*fcc*) CoO (space group: *Fm3m*, *a* = 4.261Å, ICDD 78–0431) well. No shift was observed in the peak positions of the obtained diffractogram in comparison with the XRD pattern of bulk CoO in the whole 2θ-range (20–80°), indicating that the synthesized CoO nanocrystals are not strained. The absence of any extraneous peak in the diffractogram confirms the formation of a pure nanocrystalline *fcc* CoO phase. The average crystallite size was calculated to be 7.8 nm using the Scherrer equation [47].

TEM images of the as-prepared CoO nanoparticles presented in Fig. 1b and 1c show irregularly shaped particles, which is in accordance with previous reports for the synthesis of CoO nanoparticles at 230°C with a reaction time shorter than 3 h [48,49]. A high-resolution lattice image of a single CoO particle is presented in Fig. 1c, and reveals a (111) orientation of the cubic phase, which corresponds to an interplanar spacing of *d* = 2.46 Å. EDS maps of a selected area are shown in Fig. 1e and 1f. A uniform distribution of Co and O is observed across the whole particles.

The results of the structural characterization above are consistent with previous reports regarding the synthesis of *fcc* CoO nanoparticles [50,51]. However, the mechanism by which Co(acac)$_3$ is reduced to CoO

(a)   (b)   (c)

(d)   (e)   (f)

(g)
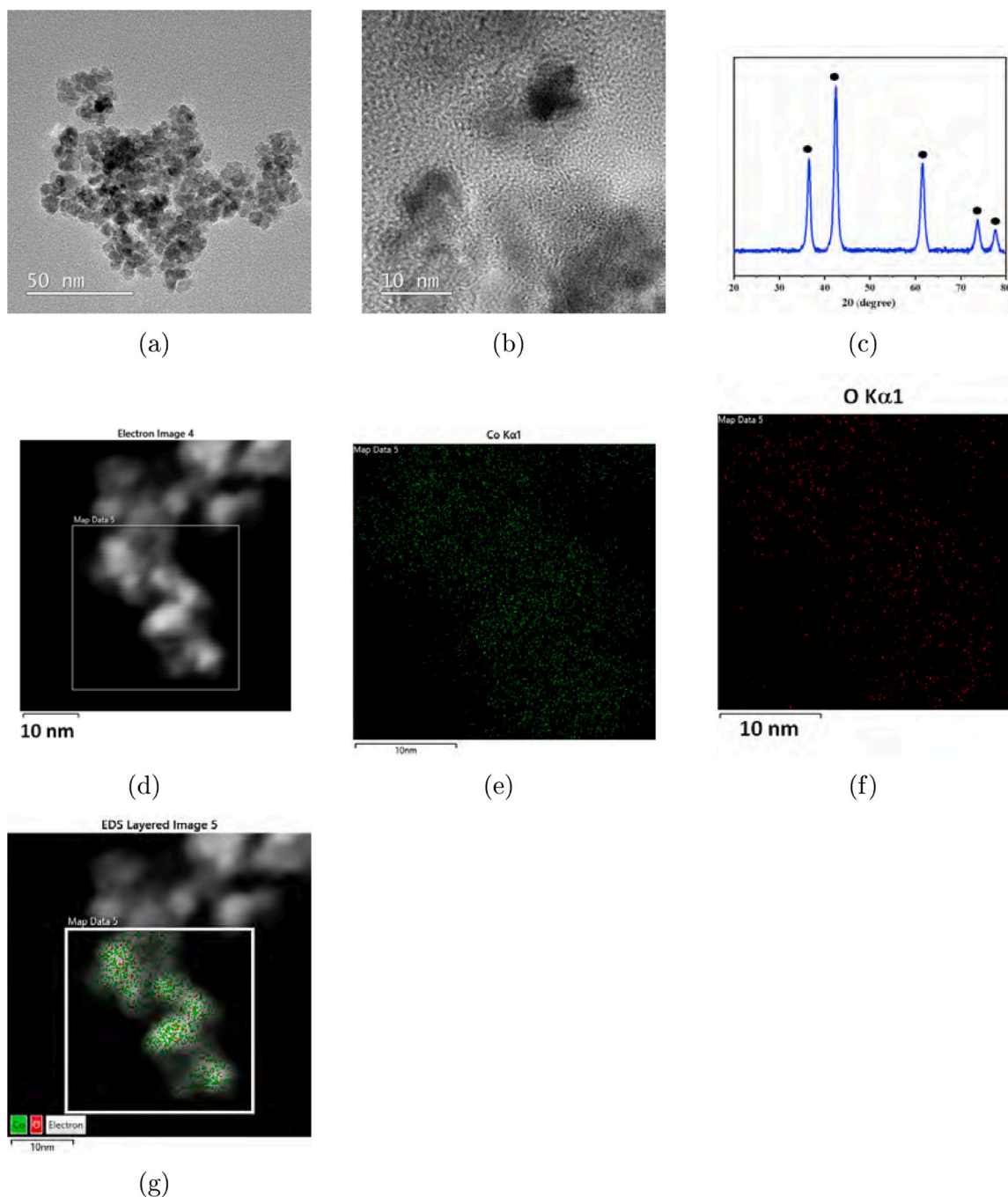
Fig. 1. (a) XRD pattern of CoO nanoparticles. (b) TEM image of as prepared CoO nanoparticles. (c) HR-TEM images of CoO nanoparticles. (d) HADAAF image of the selected area for EDS analysis. (e) and (f) Single-element TEM-EDS maps describing the distribution of Co and O respectively. (g)g Merged TEM-EDS elemental map.

and the source of oxygen has not been clearly determined. The role of the oleylamine certainly is to serve as the reducing agent and the oxygen may stem from the acetylacetonate (acac) ligand or adventitious oxygen.[1] There are several similar reports where metal oxides have been prepared by thermal decomposition of metal acetylacetonate complexes under an inert atmosphere [52–54]. It is well known that the bulk CoO exhibits *fcc* (a rocksalt-type cubic) structure, and is antiferromagnetic with a N é el temperature of ≈ 298 K [55]. However, when the particle size of CoO decreases to the nanoscale, it can also adapt a wurtzite-type hexagonal crystallite structure. The particle size and crystal structure have important influences on the magnetic properties of CoO. Hu *et al.* studied the phase- and size-dependent magnetic properties of CoO nanoparticles. They showed that the *fcc*-structured CoO was antiferromagnetic, while all the *hcp*-structured CoO samples displayed a paramagnetic behavior [51]. In our case, the absence of any response to a magnet bar, therefore, serves to show that the catalysts are antiferromagnetic which is consistent with the XRD result showing that particles have fcc structure.

3.2. Characterization of Co_xP_y nanoparticles

The XRD diffractogram of as-prepared nanoparticles (Fig. 2a)

---

[1] Tri-octyl phosphine was kept inside a glove box to prevent the formation of tri-octyl phosphine oxide.
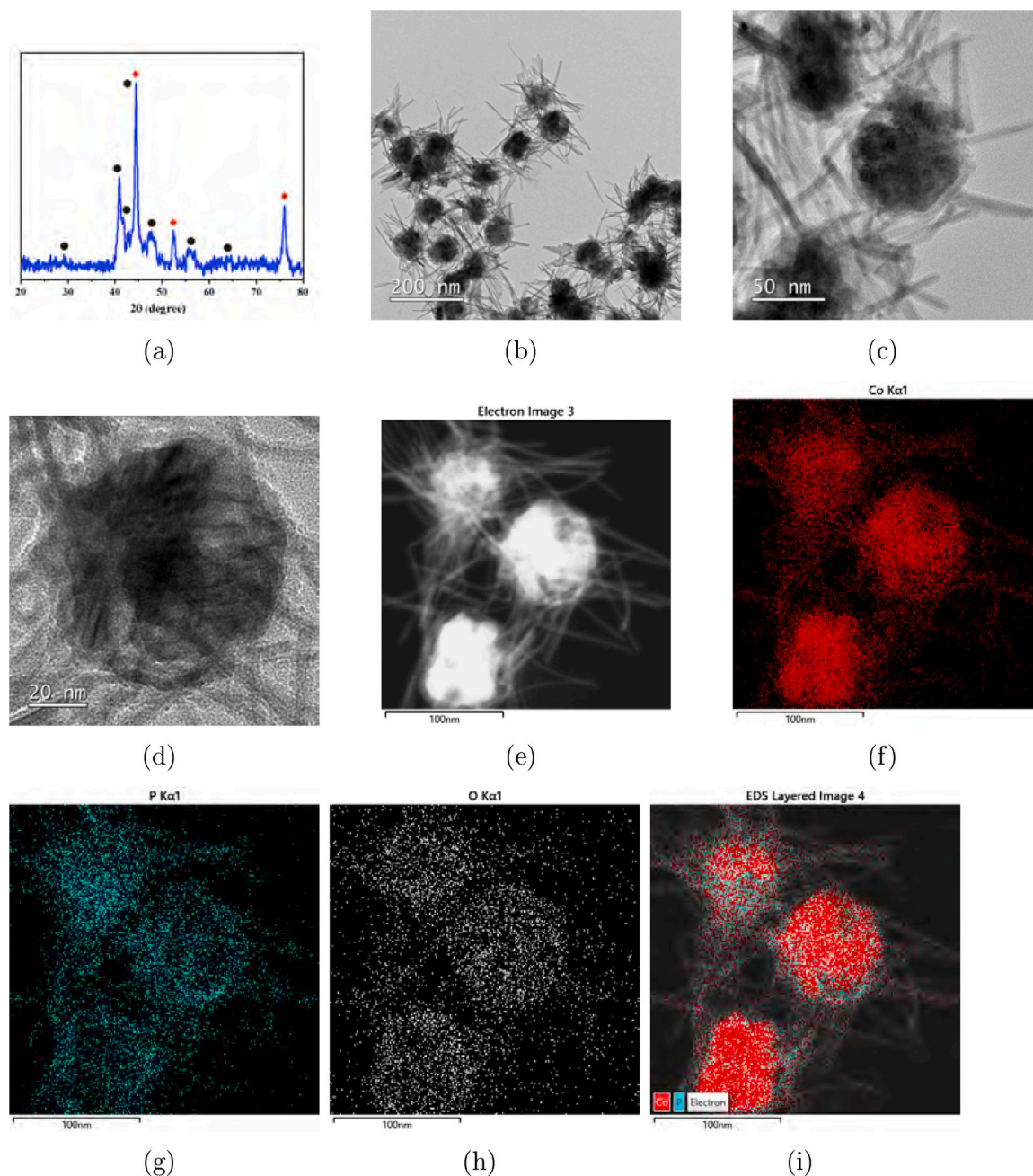
Fig. 2. (a) XRD pattern of Co_xP_y nanoparticles; red diamonds indicate the diffraction peaks of cubic Co phase and black circles indicate the diffraction peaks related to the orthorhombic Co_2P phase.(b) TEM image of as prepared Co_xP_y nanoparticles. (c) and (d) HR-TEM images of Co_xP_y nanoparticles. (e) HADAAF image of the selected area for EDS analysis. (f), (g), and (h) Single-element TEM-EDS maps describing the distribution of Co, P, and O respectively. (i) Merged TEM-EDS elemental map.

displays the diffraction peaks of orthorhombic Co_2P (ICDD 32–0306) and simple cubic cobalt Co (ICDD 15–0806) structures. The diffractions located at 44.2°, 51.5°, 75.8° and indicated with red diamonds are related to cubic Co phase and the diffraction peaks located on 40.7°, 43.2°, 44.0°, 52.0° and indicated with black circles can be identified as the (121), (211), (130), and (002) planes of Co_2P respectively.

The TEM images of as-prepared Co_xP_y nanoparticles (Fig. 2b and 2c) reveal the formation of a "sea urchin"-like nanostructure of the Co_xP_y, consisting of spherical particles in the core with multiple, needle-like protrusions that point outwards. The needle protrusions have an average diameter of 7 ± 1 nm and the average diameter of the spherical core is 58 ± 9 nm. HR-TEM images of the particles (Fig. 2d) indicate that the core is crystalline while the majority of the needles are amorphous.

The EDS spectrum in Fig. 2 was acquired for an ensemble of particles and indicates a Co:P ratio of approximately 3.8, which confirms the formation of Co-rich Co_xP_y nanoparticles. Additional EDS maps at higher resolution are included in Fig. S.1.

Although exactly this Co-rich Co_xP_y nanoparticles with "sea urchin"-like morphology has not been reported previously, a highly branched morphology has been observed for Co_2P [56], [57] nanoparticles before. Zhang *et al* [57] synthesized highly branched Co_2P nanoparticles by the thermal decomposition of cobalt(II) oleate in the presence of pure tri-octylphosphine oxide (TOPO), which was the lone phosphorus source while Popczun *et al.* [56] obtained highly branched CoO nanoparticles by using the mixture of trioctylphosphine (TOP) and TOPO. Although Popczun *et al.* [56] introduced TOPO as a prerequisite for the formation

and directing the growth of nanorod protrusions, in our protocol, such a branched morphology was obtained with just TOP as the only source of phosphorous. However, considering the mild conditions of our phosphidation step (350 °C for 30 min) a mixture of Co and Co_2P phases were obtained instead of a pure Co_2P phase.

3.3. Characterization of NiCoP nanoparticles

The XRD diffractogram of the synthesized nanoparticles is presented in Fig. 3a, which matches the Ni_2P (hexagonal) structure well. The obtained diffractogram is also in good agreement with the XRD pattern of $Co_{2-x}Ni_{x}P$ nanoparticles reported previously [49]. Therefore, all observed peaks could be assigned to the desired $(NiCo)_2P$ ternary phase. No extraneous peaks were observed, suggesting that the synthesized particles are homogeneous and without any phase impurity. The morphology, particle size, and composition of the synthesized nanoparticles were analyzed by TEM and EDS, respectively, and the results are shown through Figs. 3b, 3e, 3f, 3g, and 3h. Particles are faceted and quasi-spherical with an average size of 21 ± 2 nm, slightly larger than but comparable to values obtained from crystallite size analysis of the XRD (18 nm). The regularity of the lattice image of a nanoparticle revealed by the HR-TEM (Fig. 3c) indicates that the nanoparticles are single crystals. The space between the adjacent planes is 2.12 Å, corresponding to the (111) planes of hexagonal Ni_2P structure. The EDS mapping illustrated in Fig. 3i shows complete colocalization of Co, Ni, and P which is consistent with the formation of solid solution (alloy). Moreover, the Ni:Co ratio of the nanoparticles according to EDS analysis was found to be $\sim$ 1.1% close to the ratio employed in the synthesis.

(a)   (b)   (c)

(d)   (e)   (f)

(g)   (h)   (i)
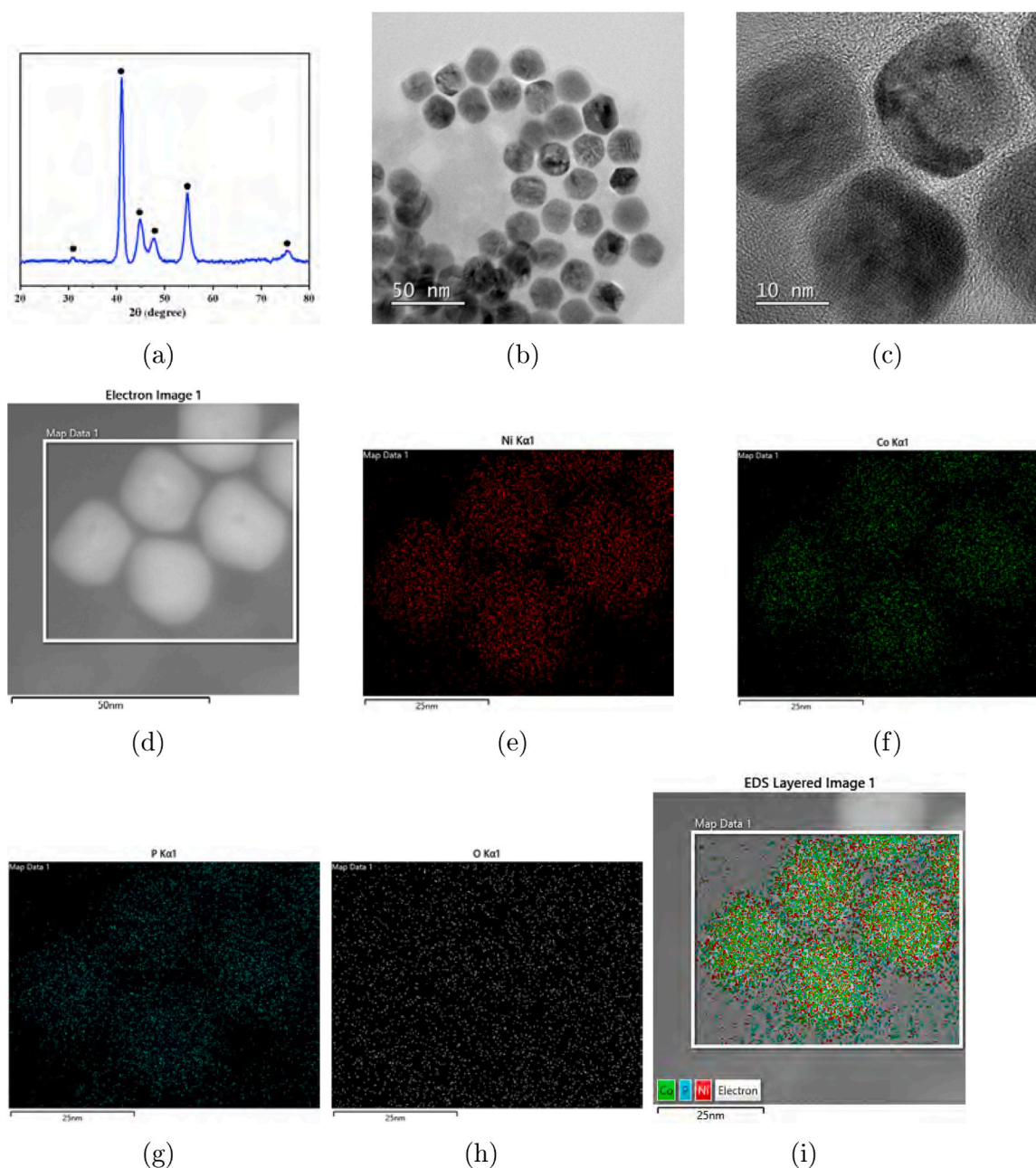
Fig. 3. (a) XRD pattern of NiCoP. (b) and (c) TEM and HR-TEM images of as prepared NiCoP nanoparticles. (d) HADAAF image of the selected area for the EDS mapping. (e), (f), (g), and (h) Single-element TEM-EDS maps describing the distribution of Ni and Co, P, and O respectively. (i) Merged TEM-EDS elemental map.
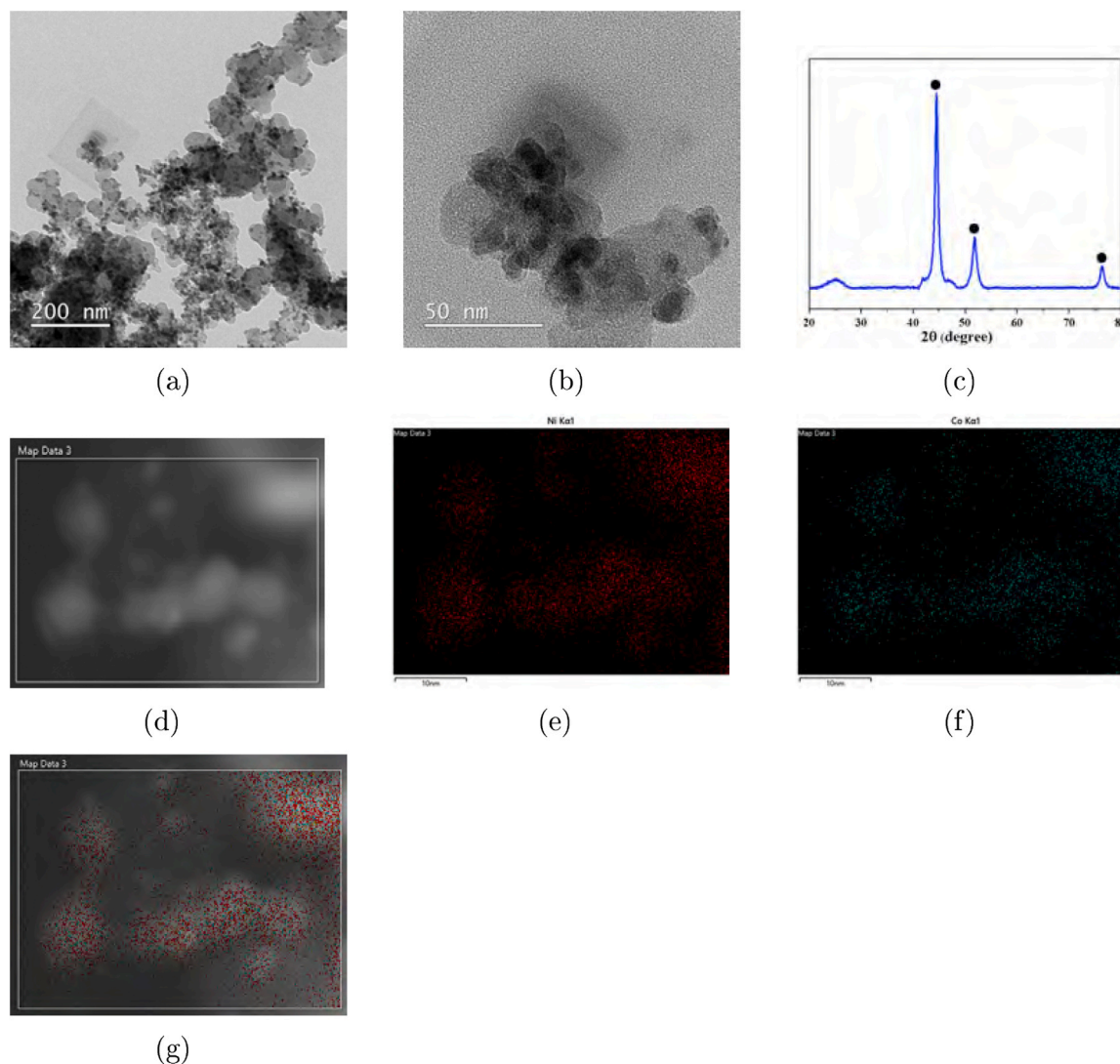
3.4. Characterization of NiCo/C nanoparticles

The XRD pattern of as-synthesized 4c NiCo/C nanoparticles shows that NiCo nanoparticles adopt the *fcc* crystallite structure. According to the phase diagram for bulk Co-Ni, alloys form over the whole range of compositions and are reported to adopt the same *fcc* structure [58]. However, it should be noted that because of the similar lattice constants of *fcc* Co and Ni and their similar atomic numbers it is not feasible to make any conclusion based on the XRD pattern to prove alloying rather than phase-segregated or core/shell structures. Therefore, the morphology, composition, and distribution of Ni and Co elements in the synthesized nanoparticles were studied using TEM and EDS mapping and the results are presented in Fig. 4. TEM images of NiCo nanoparticles are shown in Fig. 4a. The average particle size is 15 ± 2 nm. Since particles were supported on carbon, it was difficult to find a single particle to obtain a good HR-TEM image. Therefore, we were not able to study the crystallinity of the synthesized nanoparticles using HR-TEM. EDS mapping of nanoparticles showed a uniform distribution of Co and Ni atoms. However, the ratio of Ni:Co was approximately 1.8% which was higher than the targeted ratio (targeted NiCo = 1). This was in accordance with a previous report where it has been stated that in the case of using Co(acac)$_2$ Co, incorporates less efficiently than Ni. This, in turn, leads to the formation of particles with a lower amount of Co than the targeted value [59]. To obtain equimolar compositions, a larger amount of the Co precursor is necessary. Replacing the bulky acac anion in the Co salt could potentially increase the level of incorporation of Co [60].

3.5. Surface characterization of synthesized nanoparticles

The surfaces of the synthesized particles were probed with XPS. The survey spectra are shown in Fig. S.3, where all elements present in the composition of CoO, Co$_x$P$_y$, NiCoP, and NiCo/C particles were observed in their corresponding survey spectra. However, an adventitious phosphorous peak was observed in the spectrum of NiCo/C, which is due to the adsorbed TOP which has not been removed during the washing procedure [61].

Fig. 5a shows the high-resolution XPS spectra in the Co $2p$ region for all synthesized particles which comprises two main peaks attributed to Co $2p_{1/2}$ and Co $2p_{3/2}$, respectively. Despite the chemical composition of CoO, the XPS spectra were fitted with the fitting parameters for the Co$_3$O$_4$ composition. This is in accordance with previous reports for analysis of a CoO samples where it was shown that the surface of CoO is extensively oxidized to Co$_3$O$_4$ even though the bulk powder XRD spectrum showed only CoO [62–65]. However, since Co(II) and Co(III) compounds have similar binding energies [], the spectrum cannot be

(a)   (b)   (c)

(d)   (e)   (f)

(g)

Fig. 4. (a) and (b) TEM and HR-TEM images of as prepared NiCo/C nanoparticles. (c) XRD pattern of NiCoP. (d) HADAAF image of the selected area for the EDS mapping. (e), (f), (g), and (h) Single-element TEM-EDS maps describing the distribution of Ni and Co, P, and O respectively. Merged TEM-EDS elemental map.
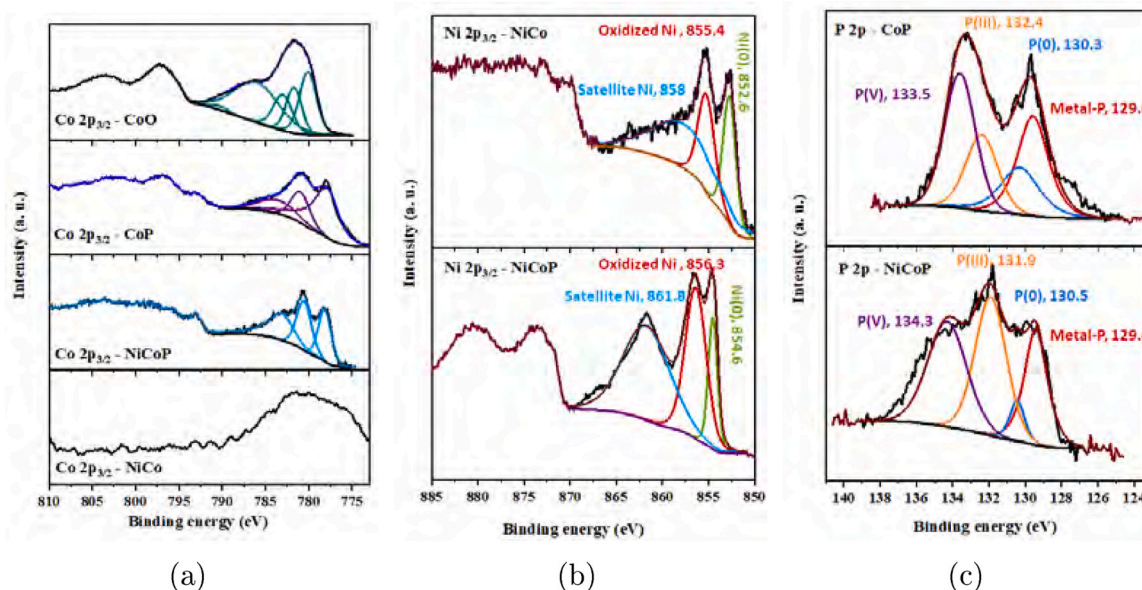
Fig. 5. Regional scans of as-prepared CoO, Co_xP_y, NiCoP, and NiCo/C nanoparticles in (a) Co2p, (b) Ni2p, and (c) P 2p regions.

used to assign the oxidation state of Co. The deconvolution of the spectra of the Co region for Co_xP_y and NiCoP was compounded by surface oxidation of nanoparticles after being stored in an ambient atmosphere. The satellite peaks for Co_xP_y, NiCoP, and NiCo are very weak. Quantification of the content of surface Co using XPS shows that there is less Co in the surface than in the bulk. Therefore a very broad peak was observed in the Co region for NiCo/C. The deconvolution of the peak was not conclusive. The binding energies observed for Ni (856.0–856.1 eV) correspond to Ni^{2+} and Ni^{3+} resulting from the oxide layer formation on the nanoparticle surface due to air exposure [66]. The peaks observed for reduced species of Ni (852.5–852.7 eV) are consistent with the binding energies reported for zerovalent Ni [67–69]. Unfortunately, Ni(0) and Ni of NiCoP are difficult to distinguish by XPS. Previous study by Li *et al.* attributed them to the same binding energies of 853.1 eV [70] while others tabulate Ni(0) at 852.7 eV and Ni_2P at 852.9 eV, only 0.2 eV apart [71].

The Ni $2p_{3/2}$ peak is slightly shifted to lower binding energies (852.7–852.5 eV) for NiCoP which has a higher amount of Co content in comparison to NiCo/C suggesting the presence of slightly higher electron density.

The XPS spectrum in the P2*p* region (Fig. 5c) shows that phosphorus species are present in the surface of the nanoparticles for NiCoP and Co_xP_y compounds. The P 2*p* region consist of four components. Each component was represented by P $2p_{3/2}$ and a higher binding energy P $2p_{1/2}$ doublet peak with a spin-orbit splitting of 0.84 eV. The P $2p_{3/2}$ binding energy is lower in these compounds than in elemental phosphorus, clearly indicating the anionic character of the P atom which is due to the transfer of electron density from the metal species to the more electronegative phosphorus. In the following, we will only indicate the binding energy of the P $2p_{3/2}$ component. For Co_xP_y (Fig. 5), components at 129.8 (red), 130.3 (blue), 132.4 (orange) and 133.6 eV (purple) were identified as an optimized combination to fit the spectrum. According to their binding energies, they were attributed to phosphide, P (0), P(III) and P(V) species respectively, based on the literature [72–74]. The same components within less than 1 eV shift were identified for NiCoP. The phosphide component was naturally attributed to cobalt phosphide and nickel cobalt phosphide species (regardless of the crystal structure). The P(0) species was barely detectable for NiCoP and slightly more intense for Co_xP_y: we tentatively propose that it corresponds to phosphorus atoms in a poorly crystallized region of the cobalt phosphides. The P(V) and P(III) components were interpreted respectively, as

surface phosphate and phosphite that may have formed as a result of the exposure of the nanoparticles to air.

3.6. Electrocatalytic activity of synthesized nanoparticles for the OER

Fig. 6a and 6b show cyclic voltammograms of CoO, Co_xP_y, (recorded between 0.9 and 1.6 V) NiCoP, and NiCo/C catalysts (recorded between 1.1 and 1.6 V) at 10 mV s^{-1} respectively in high purity 1 mol dm^{-3} SC-grade (99.99% trace metal basis) KOH. Our ICP-MS results show that even the SC-grade 0.1 mol dm^{-3} KOH contain 0.215 ppb Fe. Therefore, the contribution of Fe impurities on the results cannot be completely ruled out.

After five cycles, CoO and Co_xP_y catalysts showed a stable behavior. The cyclic voltammogram of Co_xP_y (Fig. 6a) shows two oxidation peaks (I_a) and (II_a) during the positive-going potential scan, namely at ∼ 1.13 V and ∼ 1.46 V vs. RHE, respectively. The corresponding two reduction peaks (I_c and II_c) during the negative-going potential scan appear at ∼ 1.11 V and ∼ 1.45 V, respectively. These two redox couples are assigned to the conversion between the different phases of cobalt oxides [75–77]. In case of CoO, similar to Co_xP_y two redox peaks are observed. However, only one of the redox peaks is stable after the first scan. The stable redox peak is quasi-reversible and appears at the potential close to the second (II) redox peak of Co_xP_y nanoparticles (1.45 V/1.43 V) and it is attributed to a higher Co oxide.

Similarly, the NiCoP and NiCo/C catalysts show a redox pair whose oxidation peak appears at ∼ 1.35 V and the reduction peak at ∼ 1.28 V vs. RHE). Observing a single redox peak for NiCoP and NiCo/C rather than the appearance of two distinct redox waves, i.e. one for CoO_xH_y and one for NiO_xH_y, suggests a homogeneous atomic mixing of the metal cations in a single (oxy)hydroxide phase [76].

The electrocatalytic activity of all the synthesized nanoparticles were evaluated in 1 mol dm^{-3} SC-grade (99.99% trace metal basis) KOH. As can be seen in Fig. 7, NiCo/C and NiCoP nanoparticles show a lower onset potential for the OER than CoO and Co_xP_y. At low overpotentials the catalyst performance increases in the order NiCoP> NiCo/ C> Co_xP_y> CoO and at currents larger than 25 mA cm^{-2} this order is inverted so that the activity follow the order Co_xP_y> CoO> NiCoP> NiCo/C. However, for the normalized polarization curves with respect to their double-layer capacitance the activity trend changed.

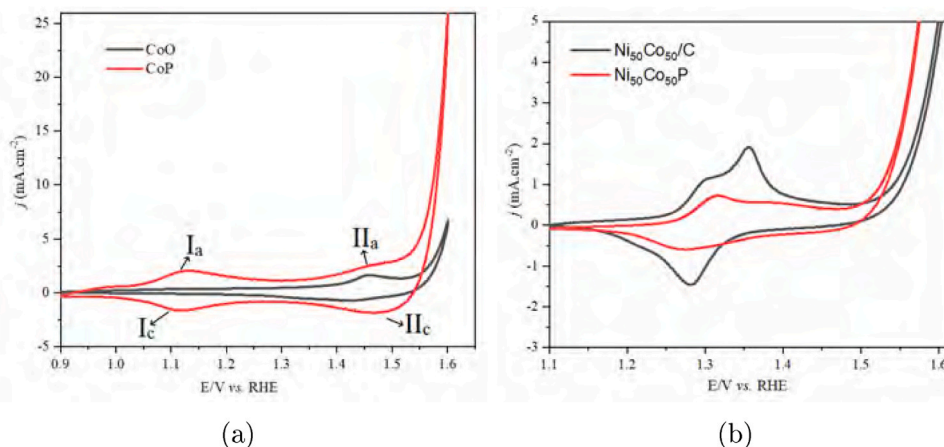Among the tested catalysts NiCoP showed the lowest overpotential

Fig. 6. Cyclic voltammograms of (a) Co_xP_y and CoO (b) NiCo/C and NiCoP catalysts at 1 mmol dm^{-3} with scan rate of 10 mVs^{-1}.
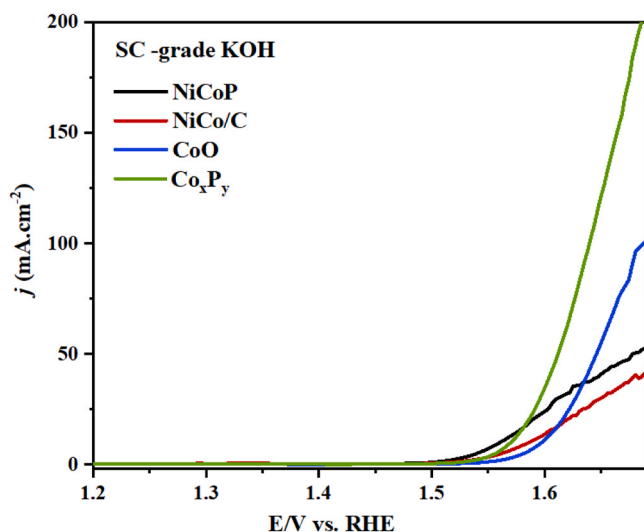
Fig. 7. LSVs CoO, Co_xP_y, NiCoP, and NiCo/C catalysts in 1 mol dm^{-3} SC-grade KOH at scan rate of 1 mV s^{-1}.

(330 mV at 10 mA cm^{-2}) while the required overpotential to reach the current density of 10 mA cm^{-2} was 350 mV, 360 mV, and 340 mV for the NiCo/C, CoO, and Co_xP_y respectively.

The overpotential η required to reach 10 and 30 mA cm^{-2}, η_{10} and η_{30}, respectively, are presented in Table 1.

Polarization curves obtained for all the catalysts are presented in Fig. 7 (The data shown were compensated for 85% of the ohmic resistance before measurements). As can be seen monometallic Co_xP_y and CoO catalysts show quite different behavior from that of bimetallic NiCo/C and NiCoP catalysts in the potential window employed. A lower potential region in which the electrode potential is approximately proportional to the logarithm of the current is seen for all compositions. However, this region is not equally extensive for all. All the tested catalysts demonstrate both the lower region and the transitioning into a

regime with a steeper Tafel slope. However, this transition to a steeper slope happens at a much lower potential for bimetallic NiCo/C and NiCoP catalysts than for monometallic Co_xP_y and CoO. Moreover, bimetallic catalysts have a well-defined transition than the monometallic catalysts. Such transition to higher Tafel slopes at more positive potentials is a frequently observed plots of electrode potentials vs. log*i* for the OER [78–81–84,85,86]. The Tafel slopes (*b*) of all the tested catalysts in the lower and higher potential region are presented in Table 1.

Electrical double-layer capacitance (C_{EDL}) was also measured for Co_xP_y, CoO, and NiCoP catalysts through cyclic voltammetry in the non-faradaic region 1.1–1.2 V (Fig. S4). NiCo/C was excluded from the double-layer capacitance measurements as the double-layer capacitance measurement method may introduce bias when carbon is present. The capacitance current was plotted vs. scan rate and the plot is shown in Fig. S4. (C_{EDL}) values of 19.77, 1.55, and 1.086 mF cm^{-2} were obtained for Co_xP_y, CoO, and NiCoP respectively. The significantly higher value obtained for Co_xP_y in comparison to CoO and Co_xP_y indicates a much higher active surface area in this catalyst which could be related to the branched (sea urchin-like) morphology of Co_xP_y nanoparticles.

Whereas there are clear differences in catalytic activity with composition (and morphology), differences in particle size (Fig. 2) may play a role. Kinoshita [87] has attributed the size effects of platinum electrocatalysts for the oxygen reduction reaction to variations in particle shape (relative fractions of facets) with size. Such effects tend to level off at a particle size around 10 nm, which are smaller than the typical size many of the catalysts in Fig. 2. These are also substantially less regular than the models employed by Kinoshita [87], and we do for these reasons not consider these models adequate for an analysis of our catalysts. Electronic effects may play a role, but again the particle size is larger than the size range in which one expects large effects of size [88]. Finally, effects of the current distribution in porous electrodes [89] may in principle lead to curves resembling those in Fig. 7. However, the thicknesses and currents involved are far too small to expect any such phenomenon in our case.

A stability test was conducted to assess the robustness of the synthesized catalysts. Cyclic voltammetry measurements were performed

Table 1
Kinetic parameters of CoO, Co_xP_y, NiCoP, NiCo/C catalysts.

Catalysts	1 dm^{-3} SC-KOH			1 dm^{-3} unpurified-KOH			1 dm^{-3} SC-KOH + 0.05 mM Fe^{3+}			1 dm^{-3} SC-KOH + 1 mM Fe^{3+}		
	η_{10}	η_{30}	**b (mV dec^{-1})**	η_{10}	η_{50}	**b (mV dec^{-1})**	η_{10}	η_{50}	**b (mV dec^{-1})**	η_{10}	η_{50}	**b (mV dec^{-1})**
Co$_x$P$_y$	335	360	58	310	354	50	300	–	40	250	–	36
CoO	360	390	47	320	360	54	320	–	53	314	–	50
NiCoP	330	383	68	310	360	54	317	–	58	284	–	42
NiCo/C	350	410	74	310	360	74	–	–	–	–	–	–

for 200 cycles, demonstrating minimal changes in the electrochemical behavior of the catalysts (Fig. S8). This finding indicates the high stability of the catalysts under the tested conditions. Note, however, that assessing the stability from cycling may be compounded by issues related other factors than the catalyst itself, such as the stability of the substrate material (glassy carbon) and the accumulation of oxygen bubbles [90].

Furthermore, we employed Raman spectroscopy to investigate the structural changes occurring in all the tested catalysts under the influence of the OER condition. Fig. S9a shows Raman spectra of as-deposited CoO, Co_xP_y, NiCoP, and NiCo/C nanoparticles on to a glassy carbon electrode (GCE). As-prepared electrodes were swept for 100 cycles between 1.1 and 1.7 V vs. RHE. Raman spectra of all tested catalysts after 100 cycles are presented in Fig. S9b. For the as-deposited films five distinct Raman peaks were observed for CoO and Co_xP_y; three peaks were observed for NiCoP and two peaks were observed for NiCo/C. These peak positions are indicated in the figures.

The observed values for the CoO peaks are close to values reported in the literature, which are typical for cubic rock-salt CoO [51]. A similar set of peaks are observed for the Co_xP_y catalyst but with a slight shift toward lower wavenumbers for all four peaks. After 100 cycles in the OER potential region, Raman spectra for the CoO and Co_xP_y catalysts remained almost the same as those prior to the cycling. As to the Raman spectra of NiCoP and NiCo/C the sharp peak at 720 cm^{-1} disappeared after OER.

3.7. Analysis of polarization curves

The polarization curves are not well described by the Tafel equation as they display only a short quasi-linear section not suitable for Tafel slope extraction and a significant upward bending at high currents. We have analyzed this upward bending in the polarization curves in terms of residual, uncompensated ohmic drops, mass transfer, gas blanketing, pH effects, and as an effect of the OER mechanism itself.

The analysis shows that it is not possible to assign the upward bending of the curves in terms of uncompensated resistance in spite of the fact that fitting the polarization data to the equation

$$i = A\exp\left[\frac{(2-\alpha)F(E - iR_\Omega)}{RT}\right] \tag{1}$$

gave reasonably good fits to the data (Fig. (S.7) in the Supporting Information). As expected for a correct compensation of ohmic resistance, the difference between the experimental data and the current predicted by the equation

$$i = A\exp\left[\frac{(2-\alpha)FE}{RT}\right], \tag{2}$$

with the parameters A, α, and R_Ω as obtained from the fit of Eq. (1), were straight lines when plotted vs. current density [91,92]. The plots are given in the Supporting Information as Fig. S.8. However, the corresponding resistances vary by one order of magnitude from data set to data set. The measured ohmic resistance (usually slightly less than 5 Ω) were very close to that computed from the formula

$$R = \frac{1}{4\kappa a} = \frac{1}{4 \times 0.2 \text{ S cm}^{-1} \times 0.25 \text{ cm}} = 5\Omega, \tag{3}$$

in which κ is the electrolyte conductivity and a the disk radius [93]. (For conductivity data see Refs. [94,95].) The potential variation is the largest close to the disk [93], 50% of it appearing closer than approximately one disk radius from the disk. Therefore the uncompensated resistance becomes less and less sensitive to the exact position of the reference electrode the further away from the disk it is placed. An experimentally observed disk resistance in close agreement with the formula, therefore, indicates that the reference electrode is far away in the sense assumed by the theory and that resistance variations from

experiment to experiment are small. We, therefore, consider variations of the order of a factor of 100 highly unlikely, and especially so given the reproducibility of the experimentally determined ohmic resistance.

This leads to the conclusion that the data are even qualitatively in disagreement with the upward bending of the polarization curves being due to uncompensated resistance; for a given resistance the current at which the curves bend upwards should be the same, as illustrated in Fig. S.9 in the Supporting Information. As is clearly visible in for example Fig. 7 this is not the case. (Similar experiments at a polycrystalline nickel disk electrode give qualitatively similar polarization curves to those in Fig. 7, but shifted to five orders of magnitude to lower currents than most active catalysts in this work. Again, the variations in resistance implied are highly unrealistic.) We, therefore, conclude that the upward bending is not due to uncompensated resistance.

For similar reasons we discard gas blanketing; also in this case one would expect the curves to bend upward at the same current which they do not. Similar conclusions were reached by Reksten et al. [78] for iridium and ruthenium oxide catalysts in acidic solutions. An effect of local pH changes near the electrode can be excluded for the same reason; a significant drop in reaction rate caused by the consumption of OH^- in the OER itself at high potentials would be expected to always happen at the same current density, which would contradict the experimental results in Fig. 8.

Finally we discard transport limitations to be the cause of the upward bending simply because the limiting current is a transport property of the electrolyte which does not depend on the properties of the catalyst; again the upward bending at different currents across five order of magnitude (if results for polcrystalline nickel are also included) is inconsistent with such a suggestions. Finally, the data even for the most active catalyst are inconsistent with a limiting current as calculated from the Levich equation, which gives

$$i_{\lim} = 0.620nFD_i^{2/3}\omega^{1/2}\nu^{-1/6}c^b = 2.5 \times 10^3 \text{ mA cm}^{-2} \tag{4}$$

In this calculation we used the diffusion coefficient corresponding to the binary (ambipolar) diffusion coefficient for a solution of KOH, i.e. from

$$D = \frac{z_{K^+}u_{K^+}D_{OH^-} - z_{OH^-}u_{OH^-}D_{K^+}}{z_{K^+}u_{K^+} - z_{OH^-}u_{OH^-}} = 2.85 \times 10^{-9} \text{ m}^2 \text{ s}^{-1} \tag{5}$$

in which we used mobilities (u_i) and diffusion coefficients (D_i) for K^+ and OH^- and at 25°C ($76.16 \times 10^{-9} \text{ m}^2 \text{ V}^{-1}\text{s}^{-1}$ and $1.957 \times 10^{-9} \text{ m}^2 \text{ s}^{-1}$ for K^+, repsectively, and $205.2 \times 10^{-9} \text{ m}^2 \text{ V}^{-1}\text{s}^{-1}$ and $5.2710^{-9} \text{ m}^2 \text{ s}^{-1}$ for OH^- respectively). (z_i is the charge number for species i.) Values for the
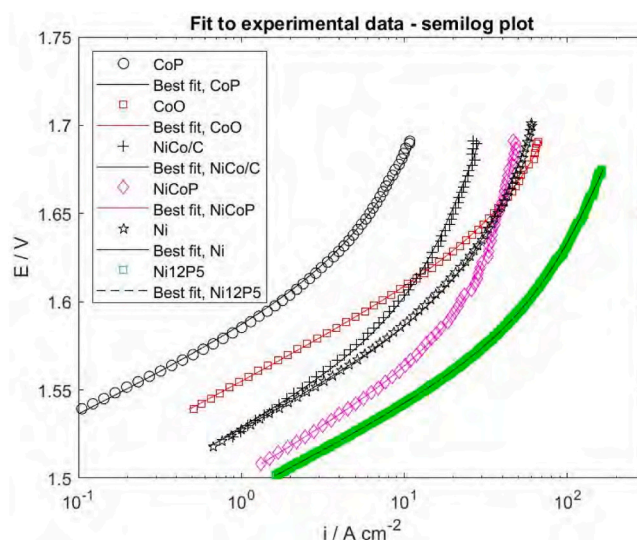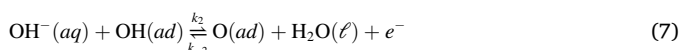

Fig. 8. Fits of Eq. (9) to experimental data. The currents were normalized with respect to the catalyst area (ECSA).

other quantities in Eq. (4) were chosen as appropriate for KOH at a concentration of 1 mol dm^{-3}. As can be seen from comparing the calculated results and the data, the upward bending cannot be associated with transport limitations in the electrolyte since the limiting current in Eq. (4) is larger than the largest current in this work by one order of magnitude and larger than the largest current for the least active catalyst by two orders of magnitude.

As neither of the attempted explanations above can rationalize the data, we next consider a microkinetic model.

3.8. Polarization curves fitting

A microkinetic steady-state model was developed for the OER through the electrochemical oxide path and the normalized polarization curve of all tested catalysts with respect to their double layer capacitance were fitted to Eq. (9) (a simplified relation for the OER Electrochemical Oxide Path) and are presented in Fig. 8.

$$S + OH^-(aq) \underset{k_{-1}}{\overset{k_1}{\rightleftharpoons}} OH(ad) + e^- \tag{6}$$

$$OH^-(aq) + OH(ad) \underset{k_{-2}}{\overset{k_2}{\rightleftharpoons}} O(ad) + H_2O(\ell) + e^- \tag{7}$$

$$O(ad) \underset{k_{-3}}{\overset{k_3}{\rightleftharpoons}} \frac{1}{2}O_2(g) + S, \tag{8}$$

$$i \approx \frac{A\exp[(1-\alpha_2)\Delta]}{1 + B\exp(-\Delta)} \tag{9}$$

in which A and B are constants (independent of potential) and Δ is the dimensionless potential $F(E-E^0)/RT$ (to which the experimental potential can be converted).

As it can be seen in Fig. 8 the fitted polarization curve describes both the high and low potential regions and the transition in between them quite well. The Tafel slopes obtained both from experimental data and from the fitting are presented in Table S.1. The results are consistent with the more complete model and indicate that the Electrochemical Oxide Path is the mechanism by which the OER proceeds for these catalysts regardless of the composition. Table S.1 includes also onset potentials for each catalyst. Onset potentials were obtained by drawing tangents in the faradaic and non-faradaic regions, then the abscissa of the point where these two tangents intersect was considered as the value of onset potential. In general, Ni containing catalysts have lower onset potential in comparison with monometallic Co catalysts, and among them, NiCoP catalyst has the lowest onset potential.

The results of EIS measurements, plotted as Tafel impedance (Z_t), at different overpotentials for CoO, Co$_x$P$_y$, and NiCoP are shown in Fig. S.6. Z_t was computed from the impedance by multiplication of the latter with the steady-state current density as [96],

$$Z_t = \frac{\widetilde{E}}{\widetilde{i}} i_{ss} \tag{10}$$

where $\widetilde{E}$ is the potential amplitude, $\widetilde{i}$ the current-density amplitude, and i_{ss} is the steady-state current density. (The ohmic resistance, as assessed from the high-frequency intercept of the impedance-plane plot with the real axis, was subtracted from all data prior to the conversion to Tafel impedance). As can be seen, the low-frequency intercept increases slightly as the overpotential is increasing. In these plots, the dE/dlogi slope can be read off as the value of the low-frequency intercept with the real axis [97,98]. For all samples, the diameter of the arc in the Tafel-impedance plane plot is in reasonable agreement with the slopes from the steady-state curves (Fig. 7) and polarization curves fitting. The Tafel slopes from the impedance data cluster around 43 mV for CoO, 40 mV for Co$_x$P$_y$, and 59 mV for NiCoP.

3.9. The effect of adventitious Fe on catalyst activity

In order to monitor the effect of the Fe adsorption on the CoO, Co$_x$P$_y$, NiCoP, and NiCo/C, the electrocatalytic activities of all these catalysts were studied in 1 mol dm^{-3} unpurified KOH and 1 mol dm^{-3} SC-grade KOH spiked with 0.05 and 1 mol dm^{-3}. Figs. 9 and 10 display the effect of these additions on the polarization curves. As it can be seen in Fig. 9, the Co$_x$P$_y$ catalyst is the one most affected by the addition of Fe. The overpotential at 10 mA cm^{-2} decreased 25 mV upon changing the electrolyte from SC-grade to unpurified KOH. Our ICP-MS results show that 0.1 mol dm^{-3} SC-grade and unpurified KOH contain 0.215 ppb and 0.620 ppb Fe, respectively. Increasing in the activity upon addition of Fe follows the trend Co$_x$P$_y$ > NiCoP > CoO. A similar trend was also observed with the addition of 0.05 and 1 mmol dm^{-3} Fe. The effect of the addition of Fe on the Ni- and Co-based nanoparticles have been intensively studied [76]. It is widely accepted that the activity of Ni-based nanoparticles increases 100-fold upon the addition of Fe while Co-based catalysts are less sensitive to Fe addition and the increase in the activity is approximately 20 fold [76]. However, our obtained results indicate that Co$_x$P$_y$ catalyst is much more sensitive to Fe than NiFeP which could be attributed to the branched morphology of Co$_x$P$_y$ and huge surface area in turn, which provides more Co sites exposed to Fe. The increase in the activity of CoO catalyst is least affected by Fe which is consistent with previous reports [76].

4. Conclusion

In this study, we have successfully synthesized and characterized CoO, Co$_x$P$_y$, NiCoP, and NiCo/C nanoparticles as catalysts for the oxygen evolution reaction (OER). The unique sea-urchin-like morphology of the Co$_x$P$_y$ nanoparticles, providing a high surface area, demonstrated superior electrocatalytic performance. Transmission electron microscopy confirmed the distinct morphologies of the synthesized nanoparticles, while X-ray diffraction analysis revealed a mixed phase of metallic cobalt and Co$_2$P for Co$_x$P$_y$, and pure phases for the other catalysts.

The electrochemical characterization, including polarization curves and a microkinetic steady-state model based on the Electrochemical Oxide Path, shed light on the OER mechanism. The fitting of the experimental polarization curves supported the proposed mechanism, and the calculated Tafel slopes were consistent with the model. This comprehensive analysis contributes to a deeper understanding of the OER process and provides valuable insights for the design and optimization of OER catalysts.
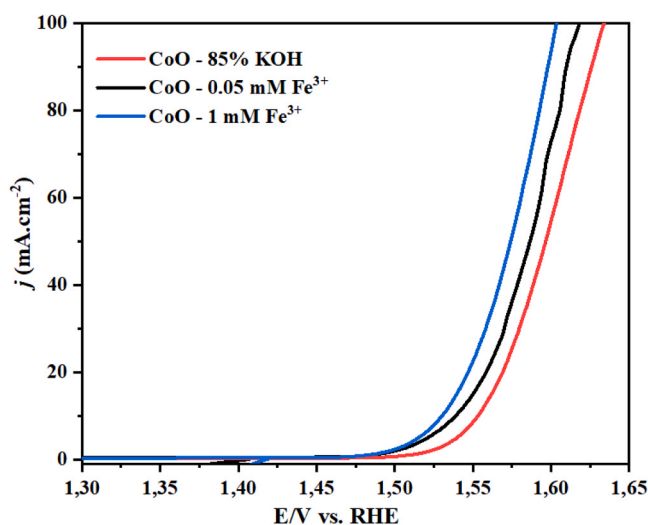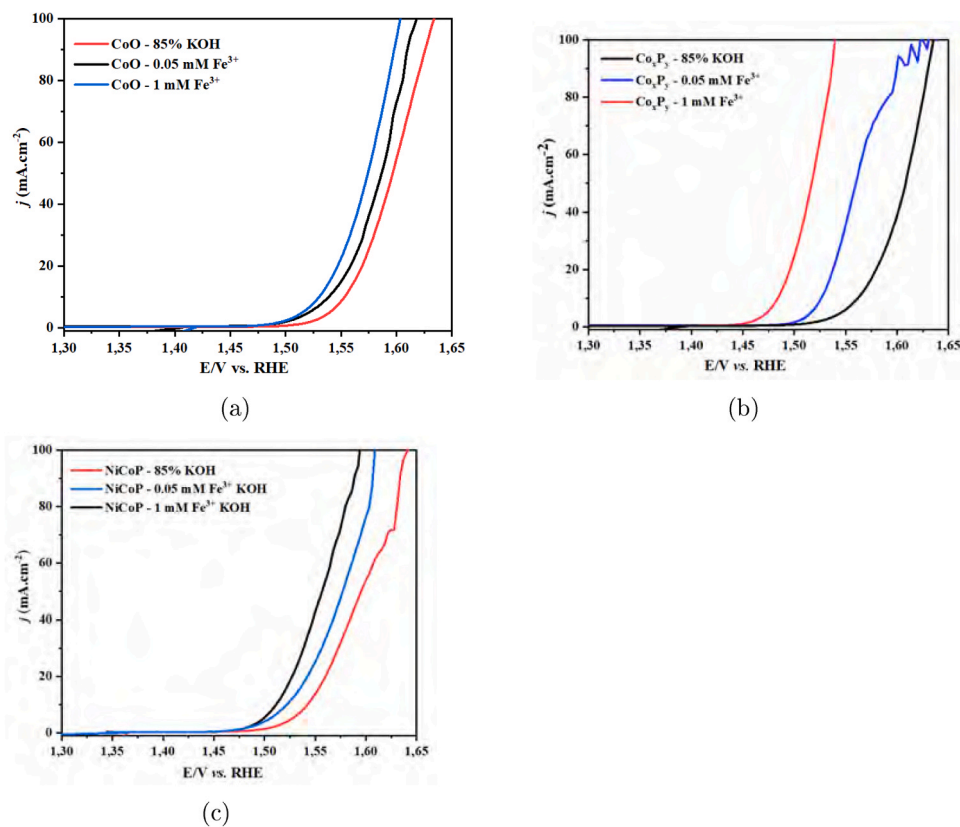

Fig. 9. LSVs of CoO, Co$_x$P$_y$, NiCoP, and NiCo/C catalysts in 1 mol dm^{-3} unpurified KOH at scan rate of 1 mV s^{-1}.

(a)

(b)

(c)

Fig. 10. LSVs of CoO, Co_xP_y and NiCoP catalysts in 1 mol dm^{-3} SC-grade KOH and in the absence and the presence of 0.05 and 1 mmol dm^{-3} spiked Fe^{3+} at scan rate of 1 mV s^{-1}.

Furthermore, the study investigated the effect of adventitious Fe on catalyst activity. Co_xP_y exhibited the highest sensitivity to Fe, highlighting the importance of the catalyst composition and morphology in determining its response to impurities. These findings have implications for the development of more efficient and durable OER catalysts for sustainable energy conversion technologies.

Overall, our work contributes to the fundamental understanding of OER catalysis and provides valuable insights for the design and optimization of advanced catalyst materials for energy conversion applications. Further research in this field can leverage these findings to develop efficient and cost-effective electrocatalysts for various energy storage and conversion systems.

CRediT authorship contribution statement

Fatemeh Poureshghi: Conceptualization, Investigation, Methodology, Writing – original draft, Writing – review & editing. **Frode Seland:** Supervision, Methodology, Writing – review & editing. **Jens Oluf Jensen:** Funding acquisition, Supervision, Methodology, Writing – review & editing. **Svein Sunde:** Funding acquisition, Conceptualization, Supervision, Methodology, Writing – review & editing, Project administration. **Megan Muriel Heath:** Acquisition of Raman Spectra presented in the supplementary information.

Declaration of Competing Interest

The authors declare that they have no known competing financial interests or personal relationships that could have appeared to influence the work reported in this paper.

Data Availability

Data will be made available on request.

Appendix A. Supporting information

Supplementary data associated with this article can be found in the online version at doi:10.1016/j.jallcom.2023.171627.

References

[1] A. Ursua, L. Gandia, P. Sanchis, Hydrogen production from water electrolysis: current status and future trends, Proc. IEEE 100 (2) (2012) 410–426, https://doi.org/10.1109/JPROC.2011.2156750. ⟨http://ieeexplore.ieee.org/ielx5/5/6132586/05898382.pdf?tp=&arnumber=5898382&isnumber=6132586%5Cnhttp://ieeexplore.ieee.org/xpls/abs_all.jsp?arnumber=5898382⟩.

[2] M. Hassan, Y. Slimani, M.A. Gondal, M.J.S. Mohamed, S. Güner, M.A. Almessiere, A.M. Surrati, A. Baykal, S. Trukhanov, A. Trukhanov, Structural parameters, energy states and magnetic properties of the novel Se-doped NiFe2O4 ferrites as highly efficient electrocatalysts for HER, Ceram. Int. 48 (17) (2022) 24866–24876, https://doi.org/10.1016/j.ceramint.2022.05.140. ⟨https://www.sciencedirect.com/science/article/pii/S0272884222017114⟩.

[3] S. Manzoor, S.V. Trukhanov, M.N. Ansari, M. Abdullah, A. Alruwaili, A.V. Trukhanov, M.U. Khandaker, A.M. Idris, K.S. El-Nasser, T.A. Taha, Flowery ln2MnSe4 Novel Electrocatalyst Developed via Anion Exchange Strategy for Efficient Water Splitting(2022). 10.3390/nano12132209.

[4] B.M. Hunter, H.B. Gray, A.M. Müller, Earth-abundant heterogeneous water oxidation catalysts, Chem. Rev. 116 (22) (2016) 14120–14136, https://doi.org/10.1021/acs.chemrev.6b00398.

[5] S. Jung, C.C.L. McCrory, I.M. Ferrer, J.C. Peters, T.F. Jaramillo, Benchmarking nanoparticulate metal oxide electrocatalysts for the alkaline water oxidation reaction, J. Mater. Chem. A 4 (8) (2016) 3068–3076, https://doi.org/10.1039/C5TA07586F.

[6] S. Trasatti, Electrocatalysis by oxides-Attempt at a unifying approach, J. Electroanal. Chem. Interfacial Electrochem. 111 (1) (1980) 125–131, https://doi.org/10.1016/S0022-0728(80)80084-2. ⟨http://www.sciencedirect.com/science/article/pii/S0022072880800842⟩.

[7] Y. Lee, J. Suntivich, K.J. May, E.E. Perry, Y. Shao-Horn, Synthesis and Activities of Rutile IrO2 and RuO2 Nanoparticles for Oxygen Evolution in Acid and Alkaline Solutions, The, J. Phys. Chem. Lett. 3 (3) (2012) 399–404, https://doi.org/10.1021/jz2016507.

[8] W. Hu, Y. Wang, X. Hu, Y. Zhou, S. Chen, Three-dimensional ordered macroporous IrO2 as electrocatalyst for oxygen evolution reaction in acidic medium, J. Mater. Chem. 22 (13) (2012) 6010–6016, https://doi.org/10.1039/C2JM16506F.

[9] L. Trotochaud, J.K. Ranney, K.N. Williams, S.W. Boettcher, Solution-cast metal oxide thin film electrocatalysts for oxygen evolution, J. Am. Chem. Soc. 134 (41) (2012) 17253–17261, https://doi.org/10.1021/ja307507a.

[10] A. Singh, L. Spiccia, Water oxidation catalysts based on abundant 1st row transition metals, Coord. Chem. Rev. 257 (17) (2013) 2607–2622, https://doi.org/10.1016/j.ccr.2013.02.027. ⟨http://www.sciencedirect.com/science/article/pii/S0010854513000611⟩.

[11] M.V. Zdorovets, A.L. Kozlovskiy, D.I. Shlimas, D.B. Borgekov, Phase transformations in FeCo - Fe2CoO4/Co3O4-spinel nanostructures as a result of thermal annealing and their practical application, J. Mater. Sci.: Mater. Electron. 32 (12) (2021) 16694–16705, https://doi.org/10.1007/s10854-021-06226-5.

[12] J.B. Gerken, J.G. McAlpin, J.Y.C. Chen, M.L. Rigsby, W.H. Casey, R.D. Britt, S. S. Stahl, Electrochemical water oxidation with cobalt-based electrocatalysts from pH 0-14: the thermodynamic basis for catalyst structure, stability, and activity, J. Am. Chem. Soc. 133 (36) (2011) 14431–14442, https://doi.org/10.1021/ja205647m.

[13] T.Y. Ma, S. Dai, M. Jaroniec, S.Z. Qiao, Metal-organic framework derived hybrid Co3O4-carbon porous nanowire arrays as reversible oxygen evolution electrodes, J. Am. Chem. Soc. 136 (39) (2014) 13925–13931, https://doi.org/10.1021/ja5082553.

[14] A. Badruzzaman, A. Yuda, A. Ashok, A. Kumar, Recent advances in cobalt based heterogeneous catalysts for oxygen evolution reaction, Inorg. Chim. Acta 511 (2020), 119854, https://doi.org/10.1016/j.ica.2020.119854. ⟨https://www.sciencedirect.com/science/article/pii/S0020169320310537⟩.

[15] J. Han, X. Liu, H. Wan, D. Wu, G. Chen, J. Li, Y. Cao, R. Ma, Composition tuning of ultrafine cobalt-based spinel nanoparticles for efficient oxygen evolution, ACS Sustain. Chem. Eng. 8 (14) (2020) 5534–5543, https://doi.org/10.1021/acssuschemeng.9b07025.

[16] C.-Z. Yuan, S.-L. Zhong, Y.-F. Jiang, Z.K. Yang, Z.-W. Zhao, S.-J. Zhao, N. Jiang, A.-W. Xu, Direct growth of cobalt-rich cobalt phosphide catalysts on cobalt foil: an efficient and self-supported bifunctional electrode for overall water splitting in alkaline media, J. Mater. Chem. A 5 (21) (2017) 10561–10566, https://doi.org/10.1039/C7TA01776F.

[17] J. Chang, Y. Xiao, M. Xiao, J. Ge, C. Liu, W. Xing, Surface oxidized cobalt-phosphide nanorods as an advanced oxygen evolution catalyst in alkaline solution, ACS Catal. 5 (11) (2015) 6874–6878, https://doi.org/10.1021/acscatal.5b02076.

[18] M.S. Burke, L.J. Enman, A.S. Batchellor, S. Zou, S.W. Boettcher, Oxygen evolution reaction electrocatalysis on transition metal oxides and (oxy)hydroxides: activity trends and design principles, Chem. Mater. 27 (22) (2015) 7549–7558, https://doi.org/10.1021/acs.chemmater.5b03148.

[19] M. Gong, Y. Li, H. Wang, Y. Liang, J.Z. Wu, J. Zhou, J. Wang, T. Regier, F. Wei, H. Dai, An advanced ni-fe layered double hydroxide electrocatalyst for water oxidation, J. Am. Chem. Soc. 135 (23) (2013) 8452–8455.

[20] L.J. Enman, M.S. Burke, A.S. Batchellor, S.W. Boettcher, Effects of intentionally incorporated metal cations on the oxygen evolution electrocatalytic activity of nickel (oxy) hydroxide in alkaline media, Acs Catal. 6 (4) (2016) 2416–2423.

[21] L. Trotochaud, S.L. Young, J.K. Ranney, S.W. Boettcher, Nickel-iron oxyhydroxide oxygen-evolution electrocatalysts: the role of intentional and incidental iron incorporation, J. Am. Chem. Soc. 136 (18) (2014) 6744–6753.

[22] M. Görlin, P. Chernev, J. Ferreira de Araújo, T. Reier, S. Dresp, B. Paul, R. Krähnert, H. Dau, P. Strasser, Oxygen evolution reaction dynamics, faradaic charge efficiency, and the active metal redox states of Ni-Fe oxide water splitting electrocatalysts, J. Am. Chem. Soc. 138 (17) (2016) 5603–5614, https://doi.org/10.1021/jacs.6b00332.

[23] D. Friebel, M.W. Louie, M. Bajdich, K.E. Sanwald, Y. Cai, A.M. Wise, M.-j. Cheng, D. Sokaras, T.-c. Weng, R. Alonso-mori, R.C. Davis, J.R. Bargar, J.K. Nørskov, A. Nilsson, A.T. Bell, Identification of Highly Active Fe Sites in (Ni,Fe)OOH for Electrocatalytic Water Splitting(2015). 10.1021/ja511559d.

[24] N. Li, D.K. Bediako, R.G. Hadt, D. Hayes, T.J. Kempa, F. vonCube, D.C. Bell, L. X. Chen, D.G. Nocera, Influence of iron doping on tetravalent nickel content in catalytic oxygen evolving films, Proc. Natl. Acad. Sci. 114 (7) (2017) 1486 LP–1491, https://doi.org/10.1073/pnas.1620787114.

[25] A. Tseung, S. Jasem, Oxygen evolution on semiconducting oxides, Electrochim. Acta 22 (1) (1977) 31–34.

[26] S. Jasem, A. Tseung, A potentiostatic pulse study of oxygen evolution on teflon-bonded nickel-cobalt oxide electrodes, J. Electrochem. Soc. 126 (8) (1979) 1353.

[27] J. Nai, H. Yin, T. You, L. Zheng, J. Zhang, P. Wang, Z. Jin, Y. Tian, J. Liu, Z. Tang, et al., Efficient electrocatalytic water oxidation by using amorphous ni-co double hydroxides nanocages, Adv. Energy Mater. 5 (10) (2015), 1401880.

[28] X. Yan, K. Li, L. Lyu, F. Song, J. He, D. Niu, L. Liu, X. Hu, X. Chen, From water oxidation to reduction: transformation from ni x co3-x o4 nanowires to nico/nicoo x heterostructures, ACS Appl. Mater. Interfaces 8 (5) (2016) 3208–3214.

[29] H.-Y. Wang, Y.-Y. Hsu, R. Chen, T.-S. Chan, H.M. Chen, B. Liu, Ni3.-induced formation of active niooh on the spinel ni-co oxide surface for efficient oxygen evolution reaction, Adv. Energy Mater. 5 (10) (2015), 1500091.

[30] C. Zhu, D. Wen, S. Leubner, M. Oschatz, W. Liu, M. Holzschuh, F. Simon, S. Kaskel, A. Eychmüller, Nickel cobalt oxide hollow nanosponges as advanced electrocatalysts for the oxygen evolution reaction, Chem. Commun. 51 (37) (2015) 7851–7854.

[31] L. Wang, C. Lin, D. Huang, F. Zhang, M. Wang, J. Jin, A comparative study of composition and morphology effect of ni x co1-x (oh) 2 on oxygen evolution/reduction reaction, ACS Appl. Mater. Interfaces 6 (13) (2014) 10172–10180.

[32] F. Song, X. Hu, Exfoliation of layered double hydroxides for enhanced oxygen evolution catalysis, Nat. Commun. 5 (1) (2014) 1–9.

[33] H. Liang, F. Meng, M. Caban-Acevedo, L. Li, A. Forticaux, L. Xiu, Z. Wang, S. Jin, Hydrothermal continuous flow synthesis and exfoliation of nico layered double hydroxide nanosheets for enhanced oxygen evolution catalysis, Nano Lett. 15 (2) (2015) 1421–1427.

[34] B. Cui, H. Lin, J.-B. Li, X. Li, J. Yang, J. Tao, Core-ring structured nico2o4 nanoplatelets: synthesis, characterization, and electrocatalytic applications, Adv. Funct. Mater. 18 (9) (2008) 1440–1447.

[35] C. Bocca, A. Barbucci, M. Delucchi, G. Cerisola, Nickel-cobalt oxide-coated electrodes: influence of the preparation technique on oxygen evolution reaction (oer) in an alkaline solution, Int. J. Hydrog. Energy 24 (1) (1999) 21–26.

[36] S. Chen, J. Duan, M. Jaroniec, S.Z. Qiao, Three-dimensional n-doped graphene hydrogel/nico double hydroxide electrocatalysts for highly efficient oxygen evolution, Angew. Chem. Int. Ed. 52 (51) (2013) 13567–13570.

[37] M. Srivastava, M.E. Uddin, J. Singh, N.H. Kim, J.H. Lee, Preparation and characterization of self-assembled layer by layer nico2o4-reduced graphene oxide nanocomposite with improved electrocatalytic properties, J. Alloy. Compd. 590 (2014) 266–276.

[38] X. Wang, H. Xiao, A. Li, Z. Li, S. Liu, Q. Zhang, Y. Gong, L. Zheng, Y. Zhu, C. Chen, et al., Constructing nico/fe3o4 heteroparticles within mof-74 for efficient oxygen evolution reactions, J. Am. Chem. Soc. 140 (45) (2018) 15336–15341.

[39] W. Li, D. Xiong, X. Gao, L. Liu, The oxygen evolution reaction enabled by transition metal phosphide and chalcogenide pre-catalysts with dynamic changes, Chem. Commun. 55 (60) (2019) 8744–8763, https://doi.org/10.1039/c9cc02845e.

[40] J. Wang, W. Yang, J. Liu, CoP2 nanoparticles on reduced graphene oxide sheets as a super-efficient bifunctional electrocatalyst for full water splitting, J. Mater. Chem. A 4 (13) (2016) 4686–4690, https://doi.org/10.1039/C6TA00596A.

[41] L. Jiao, Y.-X. Zhou, H.-L. Jiang, Metal-organic framework-based cop/reduced graphene oxide: high-performance bifunctional electrocatalyst for overall water splitting, Chem. Sci. 7 (3) (2016) 1690–1695.

[42] J.F. Callejas, C.G. Read, C.W. Roske, N.S. Lewis, R.E. Schaak, Synthesis, characterization, and properties of metal phosphide catalysts for the hydrogen-evolution reaction, Chem. Mater. 28 (17) (2016) 6017–6044.

[43] A.S. Nugraha, G. Lambard, J. Na, M.S.A. Hossain, T. Asahi, W. Chaikittisilp, Y. Yamauchi, Mesoporous trimetallic ptpdau alloy films toward enhanced electrocatalytic activity in methanol oxidation: unexpected chemical compositions discovered by bayesian optimization, J. Mater. Chem. A 8 (27) (2020) 13532–13540, https://doi.org/10.1039/d0ta04096g.

[44] E. Muthuswamy, G.H.L. Savithra, S.L. Brock, Control of phase, Size, Morphol. Nickel Phosphide Nanopart. 3 (2011) 2402–2411, https://doi.org/10.1021/nn1033357.

[45] C.C.L. McCrory, S. Jung, I.M. Ferrer, S.M. Chatman, J.C. Peters, T.F. Jaramillo, Benchmarking hydrogen evolving reaction and oxygen evolving reaction electrocatalysts for solar water splitting devices, J. Am. Chem. Soc. 137 (13) (2015) 4347–4357, https://doi.org/10.1021/ja510442p.

[46] C.C.L. McCrory, S. Jung, J.C. Peters, T.F. Jaramillo, Benchmarking heterogeneous electrocatalysts for the oxygen evolution reaction, J. Am. Chem. Soc. 135 (45) (2013) 16977–16987, https://doi.org/10.1021/ja407115p.

[47] U. Holzwarth, N. Gibson, The Scherrer equation versus the 'Debye-Scherrer equation, Nat. Nanotechnol. 6 (9) (2011) 534, https://doi.org/10.1038/nnano.2011.145.

[48] M. Ghosh, E.V. Sampathkumaran, C.N.R. Rao, Synthesis and magnetic properties of CoO nanoparticles, Chem. Mater. 17 (9) (2005) 2348–2352, https://doi.org/10.1021/cm0478475.

[49] D.R. Liyanage, S.J. Danforth, Y. Liu, M.E. Bussell, S.L. Brock, Simultaneous control of composition, size, and morphology in discrete Ni2-xCoxP nanoparticles, Chem. Mater. 27 (12) (2015) 4349–4357, https://doi.org/10.1021/acs.chemmater.5b00958.

[50] H. Wang, H. Si, H. Zhao, Z. Du, L.S. Li, Shape-controlled synthesis of cobalt oxide nanocrystals using cobalt acetylacetonate, Mater. Lett. 64 (3) (2010) 408–410, https://doi.org/10.1016/j.matlet.2009.11.034.

[51] X. He, Z. Li, X. Zhang, W. Qiao, X. Song, S. Yan, W. Zhong, Y. Du, Effects of Ar/H2 annealing on the microstructure and magnetic properties of CoO nanoparticles, RSC Adv. 5 (86) (2015) 69948–69954, https://doi.org/10.1039/c5ra09723a.

[52] W.S. Seo, H.H. Jo, K. Lee, B. Kim, S.J. Oh, J.T. Park, Size-dependent magnetic properties of colloidal Mn3O4 and Mno nanoparticles, Angew. Chem. Int. Ed. 43 (9) (2004) 1115–1117, https://doi.org/10.1002/anie.200352400.

[53] A.G. Nasibulin, I.S. Altman, E.I. Kauppinen, Semiempirical dynamic phase diagrams of nanocrystalline products during copper (II) acetylacetonate vapour decomposition, Chem. Phys. Lett. 367 (5) (2003) 771–777, https://doi.org/10.1016/S0009-2614(02)01795-5. ⟨https://www.sciencedirect.com/science/article/pii/S0009261402017955/⟩.

[54] W.S. Seo, H.H. Jo, K. Lee, J.T. Park, Preparation and optical properties of highly crystalline, colloidal, and size-controlled indium oxide nanoparticles, Adv. Mater. 15 (10) (2003) 795–797, https://doi.org/10.1002/adma.200304568.

[55] C.N. R. Rao, Transition-metal oxides, in: Solid state chemistry, 1974.

[56] E.J. Popczun, C.W. Roske, C.G. Read, J.C. Crompton, J.M. McEnaney, J.F. Callejas, N.S. Lewis, R.E. Schaak, Highly branched cobalt phosphide nanostructures for hydrogen-evolution electrocatalysis, J. Mater. Chem. A 3 (10) (2015) 5420–5425, https://doi.org/10.1039/C4TA06642A.

[57] H. Zhang, D.-H. Ha, R. Hovden, L.F. Kourkoutis, R.D. Robinson, Controlled synthesis of uniform cobalt phosphide hyperbranched nanocrystals using Tri-n-octylphosphine oxide as a phosphorus source, Nano Lett. 11 (1) (2011) 188–197, https://doi.org/10.1021/nl103400a.

[58] T. Nishizawa, K. Ishida, The Co-Ni (Cobalt-Nickel) system, Bull. Alloy Phase Diagr. 4 (4) (1983) 390–395, https://doi.org/10.1007/BF02868090.

[59] K.E. Marusak, A.C. Johnston-Peck, W.-C. Wu, B.D. Anderson, J.B. Tracy, Size and composition control of CoNi nanoparticles and their conversion into phosphides, Chem. Mater. 29 (7) (2017) 2739–2747, https://doi.org/10.1021/acs.chemmater.6b04335.

[60] N. Gálvez, E. Valero, M. Ceolin, S. Trasobares, M. López-Haro, J.J. Calvino, J. M. Domínguez-Vera, A. Bioinspired, Approach to the synthesis of bimetallic CoNi nanoparticles, Inorg. Chem. 49 (4) (2010) 1705–1711, https://doi.org/10.1021/ic902128g.

[61] L.M. Moreau, D.-h.H. Ha, C.R. Bealing, H. Zhang, R.G. Hennig, R.D. Robinson, Unintended phosphorus doping of nickel nanoparticles during synthesis with TOP: a discovery through structural analysis, Nano Lett. 12 (9) (2012) 4530–4539, https://doi.org/10.1021/nl301642g.

[62] M. Behazin, M.C. Biesinger, J.J. Noël, J.C. Wren, Comparative study of film formation on high-purity Co and Stellite-6: Probing the roles of a chromium oxide layer and gamma-radiation, Corros. Sci. 63 (2012) 40–50, https://doi.org/10.1016/j.corsci.2012.05.007. ⟨http://www.sciencedirect.com/science/article/pii/S0010938×12002430⟩.

[63] D. Cabrera-German, G. Gomez-Sosa, A. Herrera-Gomez, Accurate peak fitting and subsequent quantitative composition analysis of the spectrum of Co 2p obtained with Al Kα radiation: I: cobalt spinel, Surf. Interface Anal. 48 (5) (2016) 252–256, https://doi.org/10.1002/sia.5933.

[64] D. Briggs, Handbook of X-ray photoelectron spectroscopy, in: C.D. Wanger, W. M. Riggs, L.E. Davis, J.F. Moulder, G.E. Muilenberg (Eds.), Physical Electronics Division, 3, Perkin-Elmer Corp., Eden Prairie, Minnesota, USA, 1979. 190$195, Surface and Interface Analysis, 1981, https://doi.org/10.1002/sia.740030412.

[65] J. Yang, H. Liu, W.N. Martens, R.L. Frost, Synthesis and characterization of cobalt hydroxide, cobalt oxyhydroxide, and cobalt oxide nanodiscs, J. Phys. Chem. C. 114 (1) (2010) 111–119, https://doi.org/10.1021/jp908548f.

[66] T.I. Korányi, Phosphorus promotion of Ni (Co)-containing Mo-free catalysts in thiophene hydrodesulfurization, Appl. Catal. A: Gen. 239 (1) (2003) 253–267, https://doi.org/10.1016/S0926-860X(02)00390-3.

[67] S.J. Sawhill, K.A. Layman, D.R. Van Wyk, M.H. Engelhard, C. Wang, M.E. Bussell, Thiophene hydrodesulfurization over nickel phosphide catalysts: effect of the precursor composition and support, J. Catal. 231 (2) (2005) 300–313, https://doi.org/10.1016/j.jcat.2005.01.020. ⟨http://www.sciencedirect.com/science/article/pii/S0021951705000278⟩.

[68] S.J. Sawhill, D.C. Phillips, M.E. Bussell, Thiophene hydrodesulfurization over supported nickel phosphide catalysts, J. Catal. 215 (2) (2003) 208–219, https://doi.org/10.1016/S0021-9517(03)00018-6. ⟨http://www.sciencedirect.com/science/article/pii/S0021951703000186⟩.

[69] A.W. Burns, K.A. Layman, D.H. Bale, M.E. Bussell, Understanding the relationship between composition and hydrodesulfurization properties for cobalt phosphide catalysts, Appl. Catal. A: Gen. 343 (1) (2008) 68–76, https://doi.org/10.1016/j.apcata.2008.03.022. ⟨http://www.sciencedirect.com/science/article/pii/S092686 0×08001890⟩.

[70] H. Li, H. Li, W.-L. Dai, W. Wang, Z. Fang, J.-F. Deng, XPS studies on surface electronic characteristics of Ni-B and Ni-P amorphous alloy and its correlation to their catalytic properties, Appl. Surf. Sci. 152 (1) (1999) 25–34, https://doi.org/10.1016/S0169-4332(99)00294-9. ⟨http://www.sciencedirect.com/science/article/pii/S0169433299002949⟩.

[71] P.E.R. Blanchard, A.P. Grosvenor, R.G. Cavell, A. Mar, X-ray photoelectron and absorption spectroscopy of metal-rich phosphides M2P and M3P (M = Cr-Ni), Chem. Mater. 20 (22) (2008) 7081–7088, https://doi.org/10.1021/cm802123a.

[72] C.E. Myers, H.F. Franzen, J.W. Anderegg, X-ray photoelectron spectra and bonding in transition-metal phosphides, Inorg. Chem. 24 (12) (1985) 1822–1824, https://doi.org/10.1021/ic00206a025.

[73] S. Moldovan, A. Miche, A.-m. Nguyen, M. Bahri, O. Ersen, N. Me, D. France, L.D. Chimie, D. Matie, Bimetallic Phosphide (Ni, Cu) 2 P Nanoparticles by Inward Phosphorus Migration and Outward Copper Migration (2019). 10.1021/acs.chemmater.9b01505.

[74] S. Carenco, Z. Liu, M. Salmeron, The birth of nickel phosphide catalysts: monitoring phosphorus insertion into nickel, ChemCatChem 9 (12) (2017) 2318–2323, https://doi.org/10.1002/cctc.201601526.

[75] I.M. Sadiek, A.M. Mohammad, M.E. El-Shakre, M.I. Awad, M.S. El-Deab, B. E. Anadouli, Electrocatalytic evolution of oxygen gas at cobalt oxide nanoparticles modified electrodes, Int. J. Electrochem. Sci. 7 (4) (2012) 3350–3361.

[76] M.B. Stevens, L.J. Enman, E.H. Korkus, J. Zaffran, C.D.M. Trang, J. Asbury, M. G. Kast, M.C. Toroker, S.W. Boettcher, M. Science, T. Nancy, S. Grand, T. Energy, P. Technion, Ternary Ni-Co-Fe oxyhydroxide oxygen evolution catalysts: Intrinsic activity trends, electrical conductivity, and electronic band structure, Nano Res. 12 (9) (2019) 2288–2295, https://doi.org/10.1007/s12274-019-2391-y.

[77] M. Pontinha, S. Faty, M. Walls, M. Ferreira, M.D.C. Belo, Electronic structure of anodic oxide films formed on cobalt by cyclic voltammetry, Corros. Sci. 48 (10) (2006) 2971–2986.

[78] A.H. Reksten, H. Thuv, F. Seland, S. Sunde,The oxygen evolution reaction mechanism at Ir x Ru 1 - x O 2 powders produced by hydrolysis synthesis,Journal of Electroanalytical Chemistry 819 (July 2017) (2018)547–561.10.1016/j.jelechem.2018.04.018.

[79] A. Damjanovic, A. Dey, J. Bockris, Kinetics of oxygen evolution and dissolution on platinum electrodes, Electrochim. Acta 11 (7) (1966) 791–814, https://doi.org/10.1016/0013-4686(66)87056-1. ⟨http://www.sciencedirect.com/science/article/pii/0013468666870561⟩.

[80] A. Damjanovic, M. Genshaw, J. Bockris, The role of hydrogen peroxide in oxygen reduction at platinum in h 2 so 4 solution, J. Electrochem. Soc. 114 (5) (1967) 466.

[81] A. Hrussanova, E. Guerrini, S. Trasatti, Thermally prepared ti/rhox electrodes iv: O2 evolution in acid solution, J. Electroanal. Chem. 564 (2004) 151–157.

[82] T. Reier, H.N. Nong, D. Teschner, R. Schlögl, P. Strasser, Electrocatalytic oxygen evolution reaction in acidic environments - reaction mechanisms and catalysts, Adv. Energy Mater. 7 (1) (2017), 1601275, https://doi.org/10.1002/aenm.201601275.

[83] E. Guerrini, H. Chen, S. Trasatti, Oxygen evolution on aged iro x/ti electrodes in alkaline solutions, J. Solid State Electrochem. 11 (7) (2007) 939–945.

[84] R. Doyle, M. Lyons, Kinetics and mechanistic aspects of the oxygen evolution reaction at hydrous iron oxide films in base, J. Electrochem. Soc. 160 (2) (2013) H142.

[85] J.O. Bockris, T. Otagawa, Mechanism of oxygen evolution on perovskites, J. Phys. Chem. 87 (15) (1983) 2960–2971, https://doi.org/10.1021/j100238a048.

[86] J.O. Bockris, The electrocatalysis of oxygen evolution on perovskites, J. Electrochem. Soc. 131 (2) (1984) 290, https://doi.org/10.1149/1.2115565.

[87] K. Kinoshita, Particle-size effects for oxygen reduction on highly dispersed platinum in acid electrolytes, J. Electrochem. Soc. 137 (3) (1990) 845–848, https://doi.org/10.1149/1.2086566.

[88] R. Memming, Semiconductor Electrochemistry, Wiley-VCH, Weinheim, 2001, pp. 268–269.

[89] J.S. Newman, Electrochemical systems. Englewood Cliffs (NJ), Prentice Hall, 1992, p. 468.

[90] H.A. El-Sayed, A. Weiß, L.F. Olbrich, G.P. Putro, H.A. Gasteiger, OER catalyst stability investigation using RDE technique: a stability measure or an artifact? J. Electrochem. Soc. 166 (8) (2019) F458–F464, https://doi.org/10.1149/2.0301908jes.

[91] C. De Pauli, S. Trasatti, Composite materials for electrocatalysis of o-2 evolution: IrO2+SnO2 in acid solution, J. Electroanal. Chem. 538 (SI) (2002) 145–151, https://doi.org/10.1016/S0022-0728(02)01055-0.

[92] L.-E. Owe, M. Tsypkin, K.S. Wallwork, R.G. Haverkamp, S. Sunde, Iridium-ruthenium single phase mixed oxides for oxygen evolution: composition dependence of electrocatalytic activity, Electrochim. Acta 70 (0) (2012) 158–164, https://doi.org/10.1016/j.electacta.2012.03.041. ⟨http://www.sciencedirect.com/science/article/pii/S0013468612003805⟩.

[93] J. NEWMAN, Resistance for flow of current to a disk, 501-&, J. Electro Soc. 113 (5) (1966), https://doi.org/10.1149/1.2424003.

[94] M. Schalenbach, A.R. Zeradjanin, O. Kasian, S. Cherevko, K.J.J. Mayrhofer, A perspective on low-temperature water electrolysis - challenges in alkaline and acidic technology, Int. J. Electrochem. Sci. 13 (2) (2018) 1173–1226, https://doi.org/10.20964/2018.02.26.

[95] R.J. Gilliam, J.W. Graydon, D.W. Kirk, S.J. Thorpe, A review of specific conductivities of potassium hydroxide solutions for various concentrations and temperatures, Int. J. Hydrog. Energy 32 (3) (2007) 359–364, https://doi.org/10.1016/j.ijhydene.2006.10.062.

[96] F. Jaouen, G. Lindbergh, Transient techniques for investigating mass-transport limitations in gas diffusion electrodes: I. modeling the cathode, J. Electrochem. Soc. 150 (12) (2003) A1699.

[97] M. Darab, A.O. Barnett, G. Lindbergh, M.S. Thomassen, S. Sunde, The influence of catalyst layer thickness on the performance and degradation of PEM fuel cell cathodes with constant catalyst loading, Electrochim. Acta 232 (2017) 505–516, https://doi.org/10.1016/j.electacta.2017.02.101. ⟨https://www.sciencedirect.com/science/article/pii/S0013468617303778⟩.

[98] S.L. daSilva, E.A. Ticianelli, Studies of the limiting polarization behavior of gas diffusion electrodes with different platinum distributions and hydrophobic properties, J. Electroanal. Chem. 391 (1–2) (1995) 101–109.